UNCLASSIFIED

AD NUMBER

AD482942

NEW LIMITATION CHANGE

TO

Approved for public release, distribution
unlimited

FROM

Distribution authorized to U.S. Gov't.
agencies and their contractors; Critical
Technology; MAY 1966. Other requests shall
be referred to Air Force Weapons Lab,
Attn: WLRP, Kirtland AFB, NM 87117.

AUTHORITY

Air Force Weapons Lab ltr dtd 30 Nov 1971

THIS PAGE IS UNCLASSIFIED

AD 482942

ATTENUATION OF SHOCK WAVES IN SOLIDS

John O. Erkman

Andrew B. Christensen

G. R. Fowles

Stanford Research Institute
Menlo Park, California
Contract AF29(601)-6734

Research and Technology Division
AIR FORCE WEAPONS LABORATORY
Air Force Systems Command
Kirtland Air Force Base
New Mexico

ATTENUATION OF SHOCK WAVES IN SOLIDS

John O. Erkman

Andrew B. Christensen

G. R. Fowles

Stanford Research Institute
Menlo Park, California
Contract AF29(601)-6734

TECHNICAL REPORT NO. AFWL-TR-66-12

FOREWORD

This report has been reviewed and is approved.

GEORGE P. CROTWELL, JR.
Captain   USAF
Project Officer

CLYDE C. REYNOLDS
Lt Colonel USAF
Chief, Physics Branch

WILLIAM H. STEPHENS
Colonel   USAF
Chief, Research Division

ii

ABSTRACT

Attenuation of shock waves was studied in annealed 1060 aluminum, 2024-T351 aluminum, and Teflon by impacting samples with explosively driven aluminum plates. Free-surface velocities were measured as a function of target thickness by recording the time of flight across a known distance of a thin shim which was originally in intimate contact with the surface of the sample. A streak camera was used as the recording instrument. Experimental results are believed to be more accurate than any obtained previously. Samples of 2024-T351 aluminum were shocked to approximately 110 kbars and 340 kbars by flyer plates having velocities of about 0.125 cm/μsec and 0.33 cm/μsec, respectively. 1060 aluminum was shocked to 110 kbars and significant differences in its behavior were observed in comparison to the 2024-T351 aluminum.

Two models are discussed for representing elastoplastic stress-strain relations. One of these models permits the yield stress to be an arbitrary function of the hydrostatic pressure. The other permits both the shear modulus and the yield stress to vary arbitrarily with the strain. Results of calculations using an artificial viscosity code are given for the two models. The experimental data do not show a stepwise decrease of the free-surface velocity as predicted by the simple elastic-plastic models with a von Mises or Coulomb yield criterion. This qualitative difference is attributed to Bauschinger effect.

Results for Teflon indicate that the fluid model may be satisfactory although the data are meager and contain some inconsistencies.

CONTENTS

ILLUSTRATIONS

TABLES

SECTION I

INTRODUCTION

An accurate description of shock propagation in a solid requires knowledge of the complete constitutive relation among the stress and strain tensors and the internal energy. Although a large amount of data is available on the Hugoniot equations of state of metals and other solids, in general the data indicate only the density dependence of one stress component in compression. No information has been directly obtained concerning stress difference, or the path of the stress-strain curve upon release of pressure. Most available equation of state data are therefore sufficient only for descriptions of shock propagation in which the "fluid approximation" is adequate.

It is generally assumed that at high pressures material rigidity is unimportant so that a fluid-type equation of state suffices. Such a simplification seems reasonable; however, little experimental information exists to indicate pressure levels above which this model is accurate. A priori estimates of the adequacy of the fluid model based on zero-pressure values of material strength are not conclusive because of possible increases in strength with confining pressure.

It has been demonstrated for some metals at lower pressures that rate-independent elastoplastic theory gives a reasonably accurate description of the stress-strain path for compression.[1,2] The stress-strain path followed on release of pressure from a shocked state is less well established and seems to be complicated by the Bauschinger effect.[3,4] Unfortunately, the decay of shock waves, at least at lower pressures, may be sensitive to the exact shape of the stress-strain curve for pressure release, and direct methods for measuring this curve are experimentally difficult.

1

The work reported here is an extension of earlier work in which the decay of shock waves in several solids was observed and compared with predictions based on various assumptions concerning the pressure release curves.[5, 6, 7] This earlier work showed that rigidity is significant in all the materials studied at pressures up to at least 100 kbar. Agreement between experiment and theory was obtained in most cases by assuming an elastoplastic model and a particular functional dependence of the yield stress and the shear modulus on the pressure; this representation is not necessarily unique.

Studies on aluminum during the reporting period were aimed toward obtaining more explicit information on the variation of the shear modulus and the yield stress at high pressures, and toward obtaining accurate knowledge of the shape of the pressure-release curve in the immediate vicinity of the shocked state. In this region the elastic and plastic relief waves are most distinctly separated and one can hope to determine the shear modulus and yield stress independently.

The experiments on aluminum were conducted on material in two different initial conditions. The major portion of the work was performed with 2024-T351 in the as-received condition. Some work was also performed on type 1060 to determine whether the high pressure behavior depends significantly on the initial condition. This latter material is also of interest because it is the subject of concurrent equation of state and strain-rate studies, and because of Allison's observation that the fluid model is satisfactory at higher pressures in soft aluminum.[8]

The results of the experiments and comparisons with the associated theoretical calculations on aluminum are presented in Section IV. The model on which the calculations are based is described in Section II.

A few experiments were conducted on Teflon to compare its behavior with predictions based on a fluid model. Those results are described in Section IV-5.

Several new techniques were employed in these experiments. Descriptions of the experimental methods are given in Section III. A method for propelling reasonably stress-free, intact aluminum flyer plates at a velocity of 0.33 cm/μsec was developed and used to produce controlled shock pulses of 345 kbar in aluminum. The initial free-surface jump-off velocities were measured with good precision by means of a technique that utilizes thin foils initially in contact with the surface. Some experimentation was performed with an immersed foil fluid gage which gave some additional information about the shock pulse in an adjacent solid. [9] Appendix I shows the analysis procedure for fluid-cell experiments. In the course of analyzing these experiments, some data were obtained on the index of refraction of water at high pressure. These data are presented and discussed with relation to the Lorenz-Lorentz theoretical model in Appendix II.

SECTION II

CALCULATION OF SHOCK WAVE ATTENUATION

The attenuation experiments can be simulated by the use of a computer code. Two methods were used to solve the flow equations. One, using the method of characteristics, was restricted to cases in which rigidity was neglected. The equation of state used in this code is

$$P = A\left[\left(\frac{\rho}{\rho_0}\right)^{\gamma} - 1\right] \tag{1}$$

where P is the pressure, ρ is the density, and ρ_0 is the density at zero pressure. Values of the constants A and γ for aluminum are 0.196 Mbar and 4.1, respectively, and the initial density is 2.785 g/cc. Results of the characteristics code and Eq. (1) are labeled "fluid" in the figures, to emphasize that rigidity was neglected in the calculations.

The other method for solving the flow equations made use of the method developed by von Neumann and Richtmyer which uses an artificial viscosity to smooth discontinuities in the flow.[10] This method is more easily applied to problems in which the flow must be calculated across interfaces between different materials than is the method of characteristics. It is also more easily applied to problems involving more complicated equations of state, such as an elastoplastic relation. Situations where rigidity is neglected are handled by the use of the equation

$$P = A\mu + B\mu^2 + C\mu^3 \tag{2}$$

where $\mu = \rho/\rho_0 - 1$. In such a case, the Hugoniot and the expansion adiabats are assumed to coincide and are all described by Eq. (2).

1. The Constant Poisson's Ratio Model

The elastoplastic relation is diagrammed in Fig. 1. The hydro-static curve is represented by Eq. (2), and the upper and lower curves are given by

$$\sigma_x = P \pm \frac{2}{3} Y \tag{3}$$

where σ_x is the stress in the direction of propagation of the shock and Y is the yield stress in simple tension, i.e., twice the maximum re-solved shear stress. The upper, or loading, curve is made to coincide with the Hugoniot curve just as Eq. (1) was forced to do. Calculated results agreed more closely with experimental results when Y was made to vary with the hydrostatic pressure as
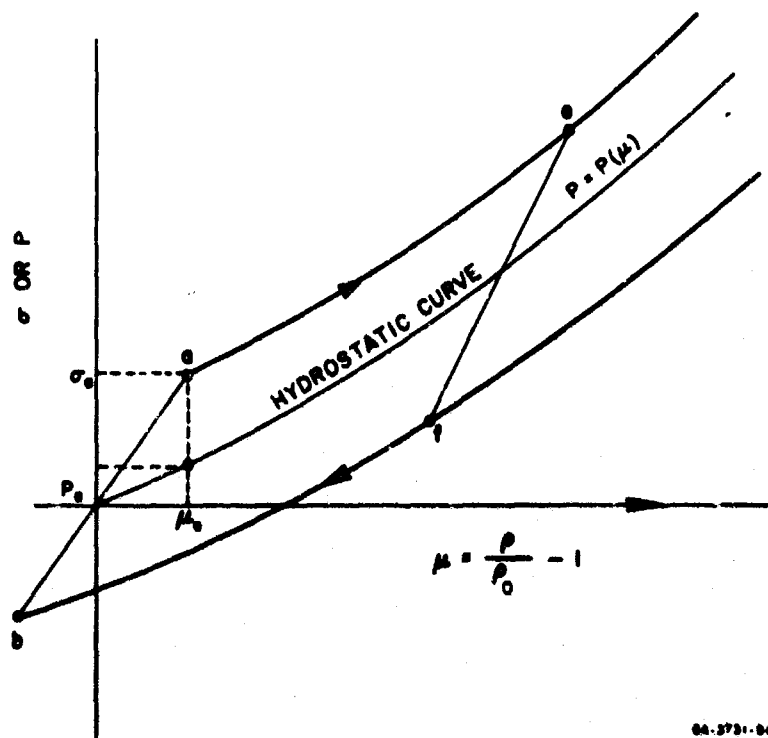
FIG. 1 SCHEMATIC DIAGRAM OF ELASTOPLASTIC STRESS-STRAIN RELATIONS

6

$$Y = Y_0 + M(P-P_a) \tag{4}$$

where Y_0 is the initial yield stress, P_a is as defined in Fig. 1, and M is a constant. Values of the various parameters for the elastoplastic equation of state are given in Table I for aluminum.

In the derivation of the elastoplastic relations, stress σ_x is related to density, ρ, by

$$d\sigma = \left(K + \frac{4}{3}G\right) \frac{d\rho}{\rho} \tag{5}$$

for an elastic event. In Eq. (5), K is the bulk modulus, G is the rigidity modulus, ρ is the density, and the subscript x has been dropped. In the constant Poisson's ratio model, K is replaced by $-V\,dP/dV$, where V is the specific volume, P is the hydrostatic pressure, and G is replaced by

$$G = 3K\frac{(1-2\nu)}{2(1+\nu)} = -\frac{3V(1-2\nu)}{2(1+\nu)}\frac{dP}{dV} \tag{6}$$

where ν is Poisson's ratio. (This model was used in most of the calculations made earlier in this and preceding projects.) Combining Eqs. (5) and (6) gives

$$\frac{d\sigma}{d\rho} = c^2 = \frac{3(1-\nu)}{(1+\nu)}\frac{dP}{d\rho} \tag{7}$$

where c is the sound speed and $dP/d\rho$ is the slope of the hydrostat. Using Eq. (3) then gives

$$c = \sqrt{\frac{3(1-\nu)}{(1+\nu)}\left[\frac{d\sigma}{d\rho} - \frac{2}{3}\frac{dY}{d\rho}\right]} \tag{8}$$

so that the elastic sound speed depends on both ν and Y. This is the speed of sound in the shocked material and is associated with the head of the rarefaction wave BM shown in Fig 2. The actual velocity of
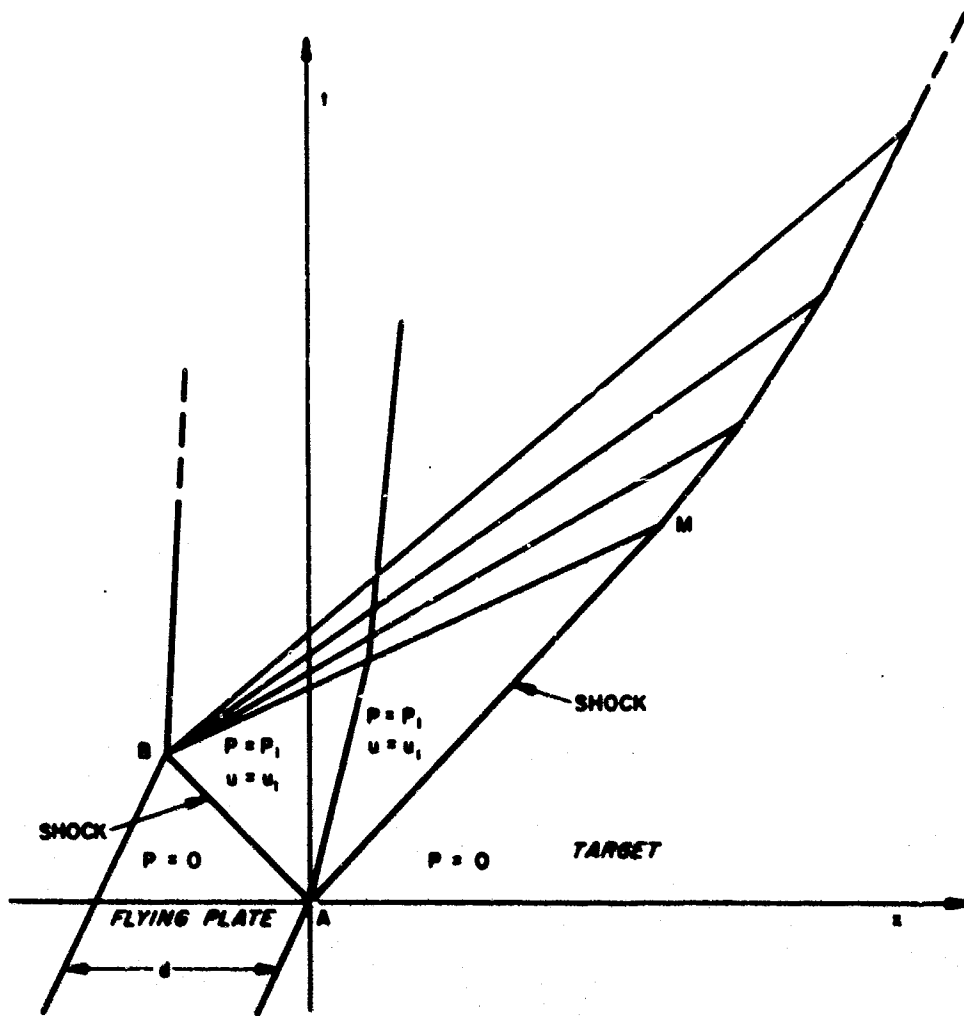
FIG. 2 PHYSICAL PLANE FOR PLATE IMPACT EXPERIMENT

this wave is $u+c$, where u is the particle velocity in the shocked region. For flyer plate experiments, the particle velocity is determined either by measuring the free-surface velocity of a thin target, or by measuring the flyer plate velocity. The latter is more desirable in principle because u is exactly one-half the flyer plate velocity, while it is only approximately half the free-surface velocity. [11] Experimentally it is easier to measure the free-surface velocity. It can be shown that the sound speed is determined if the physical coordinate of the

point M (Fig. 2) is known, [12]

$$c = (U-u)\left(\frac{x+d}{x-d}\right) \tag{9}$$

where d is the thickness of the flyer plate, x is the physical coordinate of the point M, and U is the velocity of the shock front. Because the particle velocity, u, is known, the shock velocity, U, is determined from the Hugoniot relations. Equations (8) and (9) are important links between experimental observations and the theory.

The quantity $d\sigma/d\rho$ in Eq. (8) is the slope of the Hugoniot curve from which the sound speed was obtained when calculations were done with the method of characteristics. That is, it was assumed that the expansion adiabats coincided with the Hugoniot curve for those calculations. This assumption is also made in most impedance mis-match calculations, which are frequently used in obtaining data for the Hugoniot. It is of interest to compare the elastic wave sound velocity, c_e, as given by Eq. (8) and the sound velocity from the Hugoniot. c_H. The ratio is

$$\frac{c_e}{c_H} = \sqrt{\frac{3(1-\nu)}{(1+\nu)}\left[1 - \frac{2}{3}\frac{dY}{d\sigma}\right]} \tag{10}$$

where $dY/d\sigma$ should be evaluated at a point such as e on the upper curve in Fig. 1. This means that c_e is the speed of sound at the head of the elastic wave, say the line BM in Fig. 2. The derivative can be evaluated by using Eqs. (3) and (4); the result is $M/(1+2M/3)$. For the values of M given in Table I, the derivative is small compared to 1.0. Equation (10) then gives a ratio of about 1.22 when $\nu = 1/3$, and the ratio is independent of the shock strength.

Integration of Eq. (5) with the assumptions given above gives

9

Table I

VALUES OF PARAMETERS FOR CONSTANT ν
STRESS-STRAIN RELATIONS FOR ALUMINUM

Parameters	Variable Yield Model	Constant Yield Model	Fluid Model
Y (Mbars)	0.0025	0.0025	0.0
M	0.055	0.0	0.0
ρ (g/cc)	2.785	2.785	2.785
A (Mbars)	0.755	0.743	0.765
B (Mbars)	1.29	1.74	1.86
C (Mbars)	1.197	0.329	0.428

$$\sigma_e - \sigma_f = \frac{(1-\nu)}{(1-2\nu)}(Y_e + Y_f) \tag{11}$$

where the subscripts refer to the points e and f in Fig. 1 and Y is the yield stress. For $\nu = 1/3$, and if Y does not depend strongly on the strain, the usual result

$$\sigma_e - \sigma_f = 4Y \tag{12}$$

is obtained.

The model described above has been used to calculate the stresses induced when an aluminum plate hits an aluminum target. When the velocity of the projectile is 0.125 cm/μsec, the induced stress is about 110 kbar and the calculations compare favorably with experimental results. Hence there is some validity to the model. There are, how-ever, some objections to it. One is the fact that the yield, Y, continu-ally increases with the hydrostatic pressure. With a constant value of ν, the elastic wave amplitude then continues to increase, so that fluid behavior is never approached. Another objection is the fact that G, the shear modulus, also continues to increase as $-V dP/dV$ or $\rho dP/d\rho$, so that there is no approach to fluid behavior.

Some results typical of those obtained with the constant ν model and the Q-code are given in Fig. 3. These results are for the case of an aluminum projectile 0.125-inch thick hitting a semi-infinite target. The pressure versus distance profiles are given at intervals of 1/2 μsec following projectile impact. The parameters given in column 1 of Table 1 were used in the elastoplastic stress-strain relations. In Fig. 3, the elastic relief wave reduces the amplitude of the pressure wave by about 30 kbar. Similar profiles of the particle velocity may be obtained from the calculations. Figure 4 shows only the envelope of such particle velocity profiles, along with the results of the charac-teristic code used with Eq. (1). Comparison of the two sets of results shows the early attenuation which results when the elastoplastic stress-strain relations are used. Experimental results from two previously reported experiments are included in the figure.[7]

11
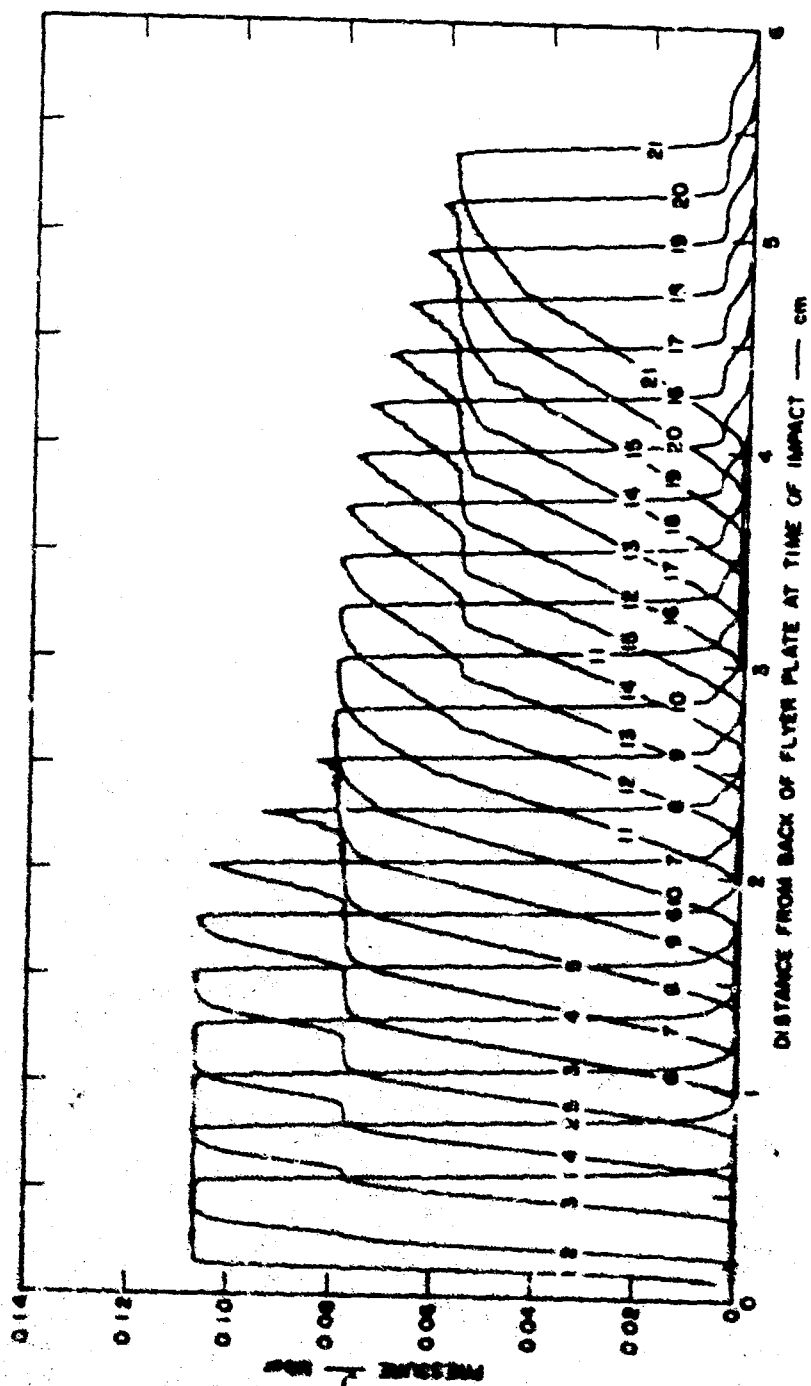
FIG. 3 PROFILES OF STRESS FOR ALUMINUM PROJECTILE HITTING AN ALUMINUM TARGET
(Projectile thickness 0.322 cm, projectile velocity 0.125 cm/µsec)
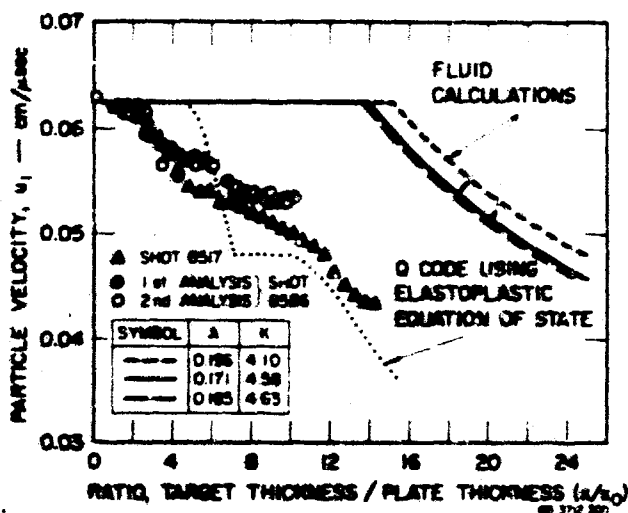
FIG. 4 PEAK PARTICLE VELOCITY IN ALUMINUM
TARGET HIT BY AN ALUMINUM PROJECTILE

2.   Variable Shear Modulus Model

It is not necessary to keep the value of Poisson's ratio constant.
If ν is permitted to increase with stress, G, the shear modulus changes
with stress in a different way from that used in the earlier calculations
(see Eq. [6]). Better understanding of the relations may result if ν is
eliminated and G is retained. Hence from Eq. (5) the elastic sound
speed is

$$c^2 = \frac{d\sigma}{d\rho} = V\left(K+\frac{4}{3}G\right) = FV \tag{13}$$

where F is called the longitudinal elastic modulus. Experiments with
flyer plates give values of both c and V, so that F may be calculated.
If experimental results are available at two or more stress levels, the
behavior of F with stress, or with strain, may be ascertained. It can
then be assumed that $K = -V\,dP/dV$ as before. so that

$$G = \frac{3}{4}(F-K) = \frac{3}{4}\left(\rho c^2 + V\frac{dP}{dV}\right) \tag{14}$$

The quantity dP/dV is not known, but because the stress, σ. is known

13

in each set of experiments, it can be approximated by $d\sigma_H/dV$ where σ_H is on the upper, or Hugoniot, curve of Fig. 1. In this way the variables G, F, and K may be evaluated from knowledge of experimentally related values of ρ and c.

Comparison of the elastic and hydrodynamic sound speeds is done as before by replacing the hydrostatic pressure with $\sigma_H - \frac{2}{3} Y$ so that Eq. (13) becomes

$$c^2 = \frac{d\sigma_H}{d\rho} - \frac{2}{3} \frac{dY}{d\rho} + \frac{4}{3} \frac{G}{\rho} \tag{15}$$

Hence the ratio of sound speeds is

$$\frac{c_e}{c_H} = \sqrt{1 + \left(\frac{4}{3} \frac{G}{\rho} - \frac{2}{3} \frac{dY}{d\rho}\right) \bigg/ \frac{d\sigma_H}{d\rho}} \tag{16}$$

where the term involving G dominates the term containing Y for low values of the stress. The results given in Section IV indicate that the ratio is about 1.22 for a 110-kbar shock and about 1.16 for a 340-kbar shock. This variable ratio is a desirable feature of the new model. The yield and the shear modulus could be made to vary in such a manner that the ratio becomes 1.0 at some stress. For the present, temperature is not included explicitly. Effects of temperature are implicit in the functional relationships of Y and G to the density.

Equation (11) now becomes

$$\sigma_e - \sigma_f = (Y_e + Y_f)\left(K + \frac{4}{3}G\right)\bigg/2G \tag{17}$$

or by the use of Eq. (13).

$$Y_e + Y_f = 1.5\left(1 - \frac{K}{\rho c^2}\right)(\sigma_e - \sigma_f) \tag{18}$$

where K can be approximated as explained above. It was expected that

14

the experiments which give ρ and c for an elastic wave would also
give, at least approximately, values of $(\sigma_e - \sigma_f)$, so that the value of
$(Y_e + Y_f)$ could be calculated. Once these values are known as, say,
functions of the volume, Eq. (3) can be used to construct a tentative
hydrostat, and the process of calculating G and $(Y_e + Y_f)$ can be
repeated. Results of such a process are given in Section IV. In anticipation of the discussion of the results it can be stated that the shear
modulus does not appear to increase indefinitely, a desirable characteristic of the model. Because the experiments fail to show a definite
separation of the elastic and plastic relief waves, the drop in stress
caused by the elastic relief wave is poorly determined. This means
that the variation of the yield stress with stress or strain is also poorly
determined.

Results obtained with the Q-code when the variable shear modulus model was used are given in Section IV. Comparison with experimental results shows that this model is also incapable of describing
the release of stress properly. The variation of both the shear modulus
and the yield stress is also discussed further in Section IV.

3.   Equation of State of Explosive Product Gases

The Q-code permits the calculation of the flow in a detonating
explosive by use of the burn fraction described by Wilkins.[13] For the
calculations used here in the development of the high velocity flyer
plate, a polytropic equation of state was used for the detonation product
gases:

$$P = (\gamma - 1) E/V \tag{19}$$

where E is the internal energy and V is the specific volume. Values
of the parameters for both Composition B and for Du Pont sheet explosive EL-506D are given in Table II.

15

Table II

EQUATION OF STATE PARAMETERS FOR COMPOSITION B AND DETASHEET EXPLOSIVES

Explosive	Initial Density (g/cc)	Detonation Velocity (cm/μsec)	Adiabatic Exponent	Energy (Mbar-cc/g)	Chapman-Jouguet Volume (cc/g)	Chapman-Jouguet Pressure (Mbar)
Detasheet	1.470	0.685	2.70	0.3373	0.496	0.186
Comp B	1.715	0.801	2.77	0.0478	0.428	0.292

SECTION III

EXPERIMENTAL METHODS

Several new techniques were developed and used in accomplishing the goals of the program. These include a method for accelerating aluminum plates to a velocity of 0.33 mm/μsec with an explosive arrangement that permits the plate to be reasonably stress-free at the time of impact on the target. In addition, a recording system was developed that permits more accurate measurement of the initial jump-off velocity of a free surface than could be achieved previously. Finally, attempts were made to adapt a fluid-cell gage developed on another project[9] to the measurement of particle-velocity profiles in aluminum; this effort was not successful. Detailed descriptions of each of these methods are presented below.

1. High Velocity Flyer Plates

Most of the previous Stanford Research Institute work on attenuation of shock waves has used aluminum plates whose velocities were about 0.12 to 0.13 cm/μsec. Impact by these plates produces stresses of about 110 kbars in aluminum targets. Some plates were also thrown at 0.19 cm/μsec;[5] later it was found that these plates were spalling.[8] One of the tasks in the current effort was to find a means of projecting aluminum plates at higher velocity in a reliable manner. Such plates would permit experimentation at higher stress levels so that, for example, the behavior of the elastic moduli with pressure could be deduced.

The 0.19 cm/μsec plates spalled partly because of the impedance mismatch between the aluminum and the brass plate. This mismatch had the useful effect that the aluminum separated from the brass to produce a free flying plate. Balchan and Cowan[14] had thrown plates from a high impedance driver plate by putting a thin layer of a low

17

impedance material, such as magnesium, between the two plates. This method was tried using a 2-inch-thick charge of Comp B to drive a sandwich of 0.5-inch-thick brass, 0.125-inch-thick magnesium (or Plexiglas), and the 0.125-inch-thick aluminum plate. The plates were tested for spalling by causing them to impact Manganin wire gages. The records showed the flat-topped wave profile characteristic of plate impact. However, the pulse was not long enough in time, and a second pulse closely followed the first. This was interpreted to mean that the plates had spalled. When the magnesium or Plexiglas layers were reduced to about 1/16-inch thick, spalling was again observed.

It was proposed that the low impedance layer between the driver and the flyer plates be replaced by explosive. This situation was investigated by the use of a computer code using the artificial viscosity method. It was soon apparent that the brass plate would have to be replaced with a softer material. When aluminum was used as the driver plate, it moved into the thin layer of explosive at a velocity close to the Chapman-Jouguet (C-J) particle velocity. The Q-code indicated that the aluminum projectile plate might spall, apparently due to the release of pressure from the back of the explosive charge--the Taylor wave. The character of the relief from the back of the charge was changed rather drastically by spacing the 2-inch-thick charge of Comp B 1.0 cm from the 0.5-inch-thick aluminum driver plate (see Fig. 5). The code indicated that this arrangement produced a flyer plate that remained intact, and that it had a velocity of 0.36 cm/μsec. The assembly was checked by doing an experiment using Du Pont Detasheet EL-506D, 0.125-inch thick. The Manganin wire gage records showed that the plates were not spalling and that the velocity of the plates was 0.32 cm/μsec.

In the attenuation studies the plates were allowed to move about 1.0 inch before impacting the targets. This permitted waves in the

18

VACUUM   C H A M B E R

STANDOFF
GLASS

ALUMINUM SHIM
ON SURFACE

SPECIMEN

ALUMINUM FLYER
0 3175 cm

2.54 cm GAP

SHEET EXPLOS'''E
0.3175 cm

1.27 cm

ALUMINUM BUFFER

AIR GAP   1 cm

SPACER

EXPLOSIVE

P-60
PLANE-WAVE
GENERATOR
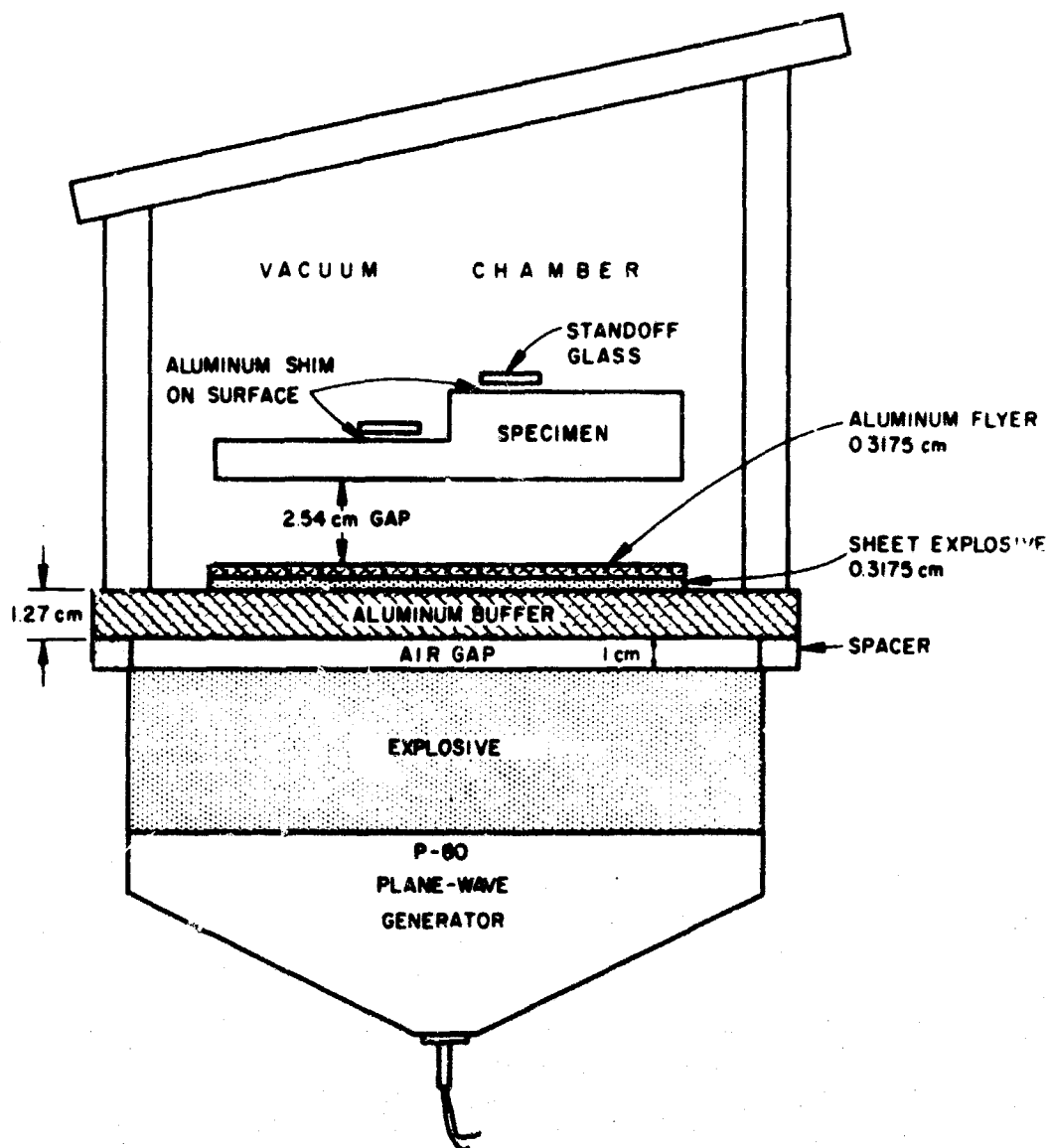
GB 5366-9

**FIG. 5 CROSS SECTION OF LAUNCHER OF HIGH SPEED ALUMINUM PLATES
AND SAMPLES**

plate to reverberate about eight times, so that approximately stress-
free conditions were reached. The explosive gases continued to exert
some pressure on the back of the flyer plates. The acceleration due
to this residual pressure has not been measured. It might have been
desirable to let the plates move farther so that waves could attenuate

19

farther and so that the gas pressure would decrease farther. However, the plates were not flat and might have been changing shape. The 1.0-inch travel was therefore a compromise.

Figure 6 shows some of the results of the calculations for the flyer plate takeoff described above. In the figure, the positions of the
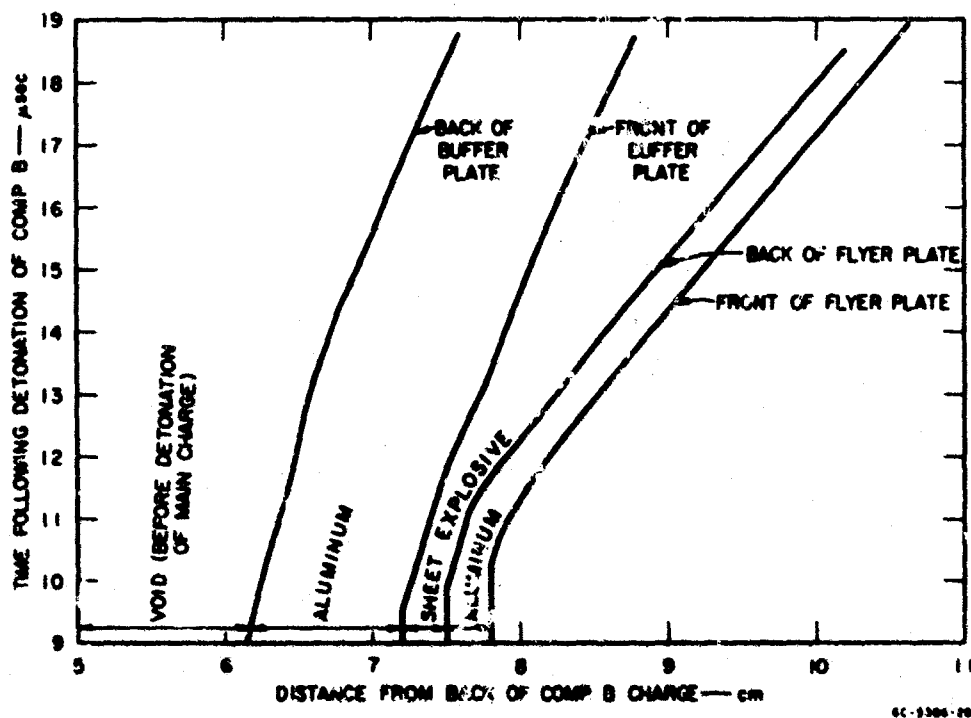
FIG. 6 TRAJECTORIES OF THE FREE SURFACE OF THE HIGH SPEED FLYER PLATE AND GAS-METAL INTERFACES (Results are from Q-code calculation. Main charge was 5-cm-thick Comp. B.)

surfaces of the two aluminum plates are given as functions of time. The flyer plate velocity changes very little after the first microsecond. The shapes of two plates are shown in Fig. 7. The plates were originally 6 inches in diameter; their shape is inferred from a streak camera record of the impact of the plates with flat glass targets. For one test, the center of the plate arrived at the glass witness plate 0.04 µsec ahead of that part of the plate on a 4-inch diameter. For another test,

20
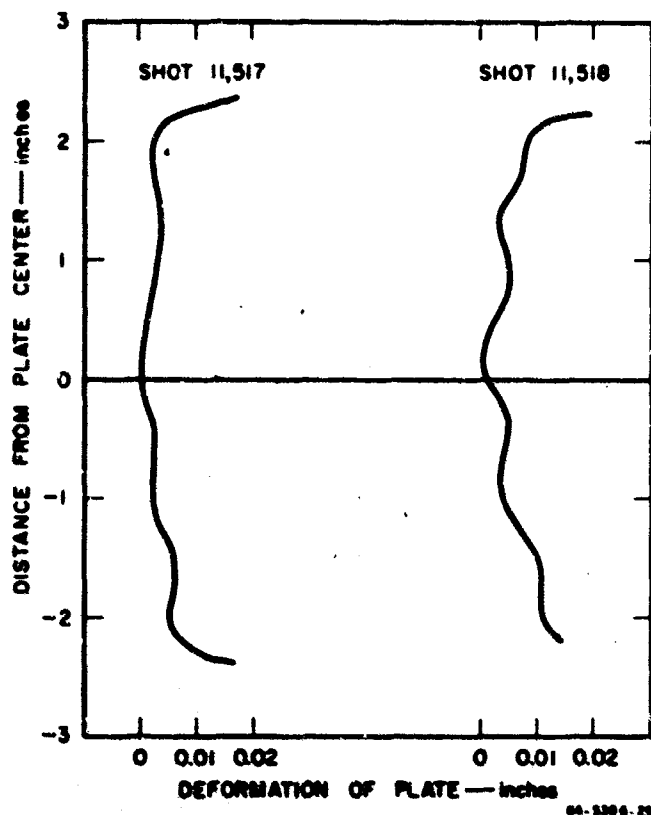
FIG. 7 RESULTS OF TESTS OF FLATNESS OF 0.325 cm/μsec
ALUMINUM FLYING PLATES

the difference in arrival time was 0.06 μsec. These differences in
time correspond to a deformation of about 0.005 to 0.008 inch, respec-
tively, across a 4-inch plate.

2. Shim Technique for Free-Surface Velocity Measurements

The free-surface velocity of a shock-loaded sample can be deter-
mined by several different methods.[19] One of the simplest is to record
the time of flight of the free surface across a gap. This method has the
disadvantage that it gives an average velocity in those cases in which
the shock is not a uniform shock, i.e., the pressure profile is not
flat-topped. What is wanted from the measurement is the velocity of
the surface at the instant of reflection of the shock wave. The

21

measurement can be made more accurately if a thin shim is held in contact with the specimen. Because the shim is made of the same material as the specimen, it acquires the same velocity as its free surface. If there is any attenuation of the shock, the surface of the specimen is decelerated while the shim continues at uniform velocity. Four samples of different thicknesses were used in each shot, as shown in the plan view of Fig. 8. The figure shows the area of each sample that was viewed by the camera through the slit and the reflections of lines in the mask that covers the light source. A cross section of the arrangement of the charge and samples is shown in Fig. 5.

For aluminum and copper, the reflectivity of the shim changes sufficiently when it is accelerated by the shock so that the take-off can be observed on the smear camera record (see lines A-A in Fig. 9). The gap is defined by a mirror (which may be partially coated with gold) set at a known distance from the original position of the shim. When the shim collides with the mirror, another change of reflectivity occurs, so the arrival can be observed in the record (lines B-B in Fig. 9). The elastic precursor wave in as-received 2024-T351 aluminum does not change the reflectivity of the shim sufficiently for the precursor to be observed. The gap closure caused by the unobserved elastic wave causes negligible error in the measurements. When annealed 2024-T351 aluminum specimens whose thickness was 0.125 inch were hit by a flyer plate of the same material (unannealed), the velocity as recorded by the shims was essentially the same as the velocity of the projectile plate. In this case the gap was about 0.19 cm, so the shim was in motion for about 1.5 μsec. During this time, relief waves from the back of the projectile plate overtook the front surface of the specimen and slowed it. The record (Fig. 9) shows the arrival of the shims at the mirrors, lines B-B, and a fraction of a microsecond later the arrival of the surface of the target, lines C-C. This illustrates the utility of

22

IMAGE OF LIGHT SOURCE
MASK AS SEEN IN SHIM

TYPICAL SAMPLE

SHIM ON SURFACE
OF SAMPLE

PROJECTION OF 3:6
SLIT ON SHOT

PROJECTION OF 2nd
SLIT ON SHOT

PROJECTION OF 1st
SLIT ON SHOT
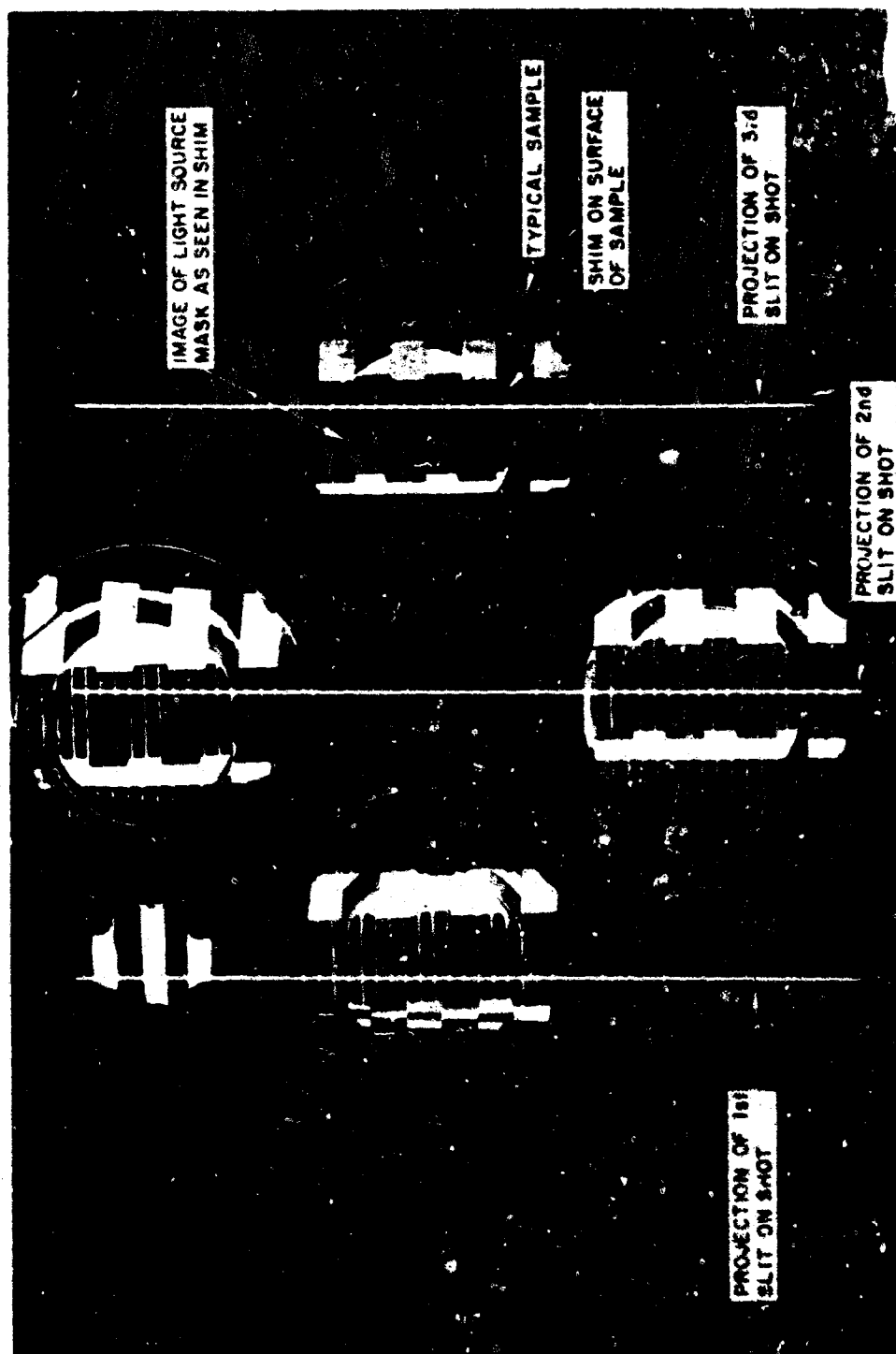
FIG. 8 PLAN VIEW OF ATTENUATION EXPERIMENT (Four samples are included in each shot)

23
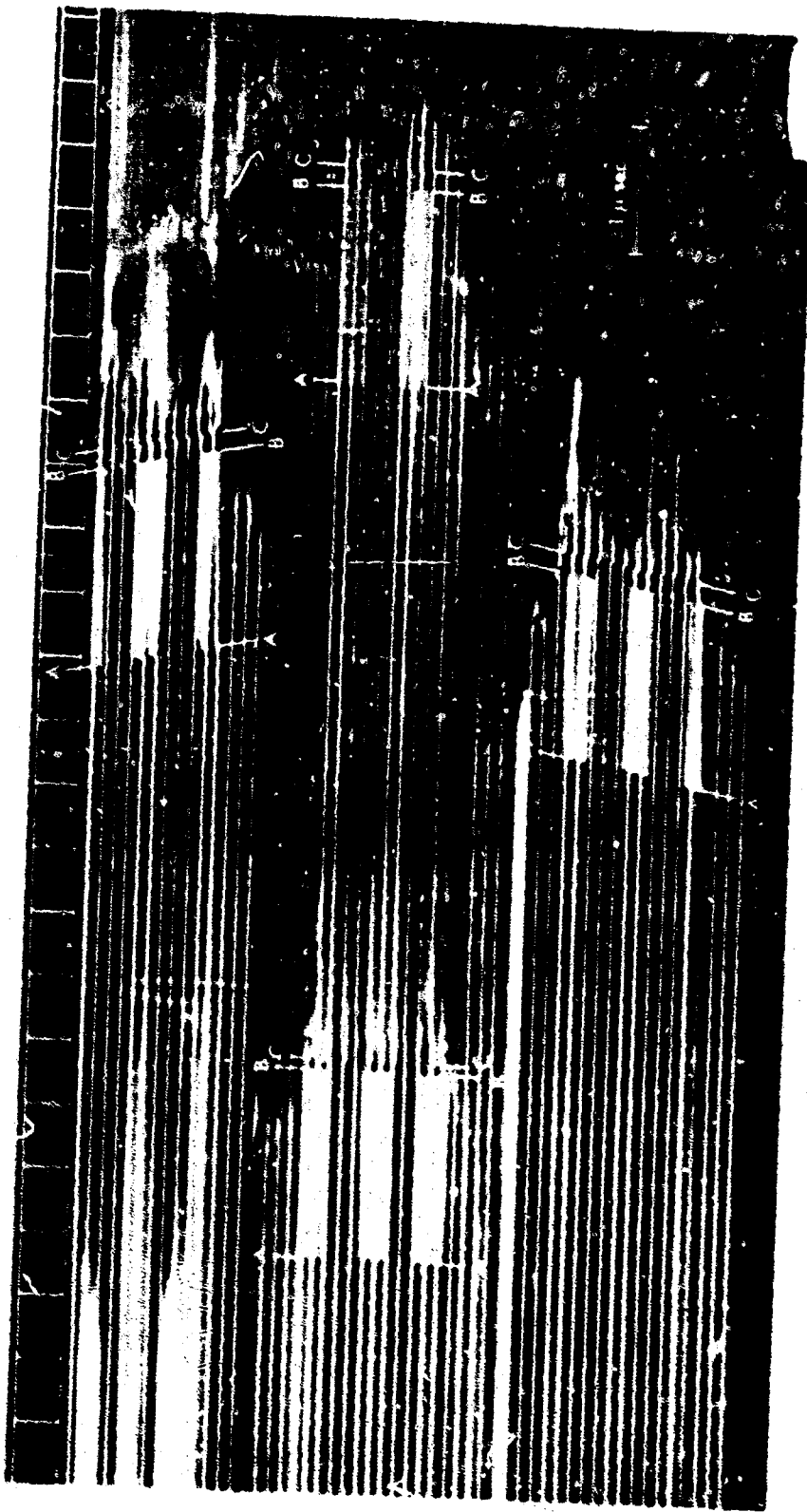
FIG. 9 TYPICAL RECORD OF ATTENUATION SHOT

24

the use of shims for the measurement of the free-surface velocity of aluminum specimens. The delay between the arrival of the shim and the target surface at the mirror depends on the thickness of the target. i.e., on the amount the shock wave has attenuated.

In the past, targets in the shape of wedges were used so that the free-surface velocity could be obtained in one experiment for a range of distances of shock travel. The optical lever arm technique was used to record the motion of the free surface. One criticism of the technique is that the shock is obliquely incident on the free surface so that the reflection of the shock results in shear waves. The analysis is also somewhat complicated, requiring the differentiation of numerical data. If truly flat flyer plates could be produced, differentiation of the data would be greatly simplified and analysis of the streak camera records would be straightforward. One of the reasons for the use of the shim technique in this program was to check results obtained previously with the optical lever arm technique.

3. **Fluid Gage**

a. **Technique**

Shock attenuation studies are concerned with the pressure or particle velocity profile of the shock wave as it changes with time in various materials. Previously the profile has been inferred with the use of both electrical gages and measurements of free-surface velocity. Use of the gages is desirable in general because, unlike free-surface measurements, they give information about the material while the pressure in the material is substantially above atmospheric. The development of the immersed Mylar foil gage provides in principle a means of measuring the shock profile in the liquid of the gage and also to some extent the profile in the driving substance.

The gage is constructed by cementing an aluminized Mylar foil
(0.00025- to 0.0005-inch thick) between rings of lucite (see Fig. 10).
This cell is mounted on the material through which the shock will prop-
agate and is oriented so that the reflecting foil is inclined to the speci-
men surface and hence the shock front at an angle α. The cell is covered
with a thin glass cover and the fluid is added so that the foil is com-
pletely immersed.
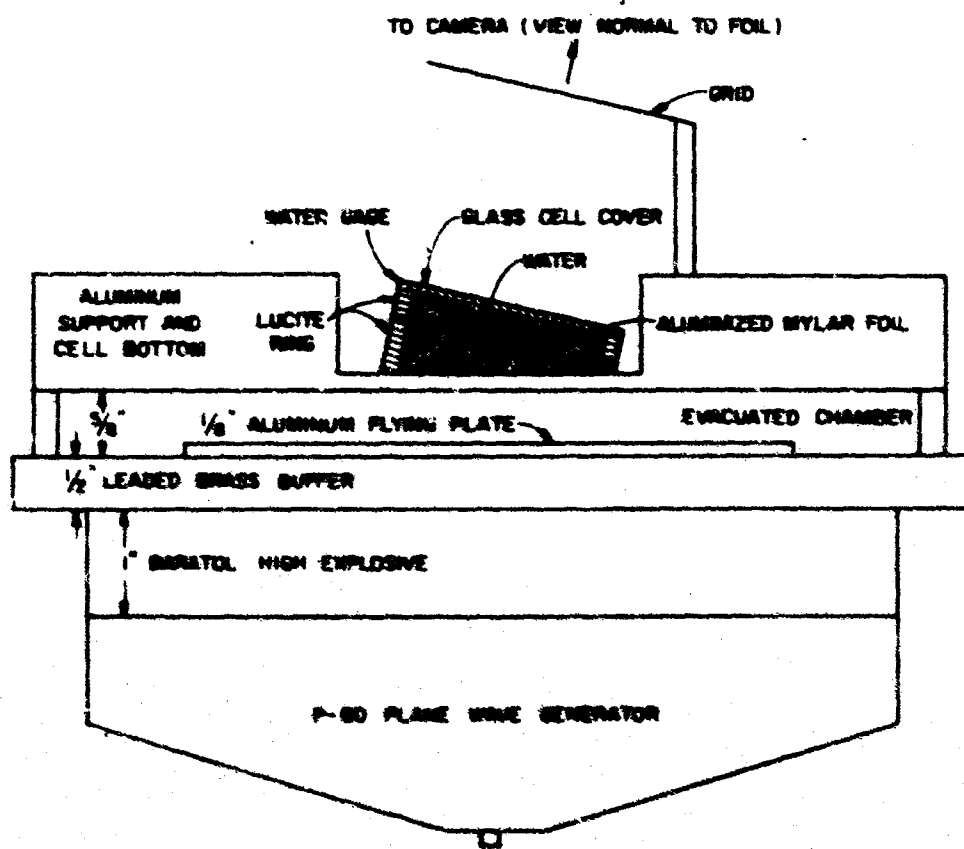
FIG. 10 WATER GAGE EXPERIMENTAL ARRANGEMENT

The fluid motion behind the shock front imparts a velocity to the
foil parallel to the shock front velocity. As a result, the foil is bent
through an angle β toward the shock front. The relationship of this
turning angle to the fluid velocity is discussed in Appendix I.

26

In practice, the optic axis is aligned perpendicular to the unturned foil. Small light sources are provided by placing a grid of alternately opaque and transparent lines over an extended light source. The camera photographs the images of these grid lines in the highly reflecting foil.

Figure 11 is an example of the streak camera record obtained using this technique. As the shock moves into the reflecting foil, the foil bends and the grid sources are then imaged in both the stationary and the moving foil. This results in a jump of the trace on the film. The magnitude of the jump and its relationship to the particle velocity in the fluid are derived in Appendix I. The position of the displaced trace is not only affected by the angle β through which the foil has turned but also by the refractive index of the shocked fluid. This is because the light rays are refracted as they pass twice through the shock front. Also of importance is the velocity of the point of intersection between the foil and the shock front. Its velocity depends on the shock velocity and the foil angle and is indicated by the slanted line, AB, across the film record.

The immersed foil gage can be utilized for several measurements, among which are: peak shock pressure in the liquid; peak shock pressure in the driver; determination of the refractive index of the shocked liquid; and observation of overtaking shocks and relief waves. It may also be possible to interpret the motion of the grid lines after jump in order to obtain information about the shock profile as a function of time.

The peak shock pressure in the liquid can be determined provided the refractive index is known. Since the foil is inclined, the pressure can be measured as a function of depth in the liquid. The reduction of the pertinent data is described in Appendix I.

27
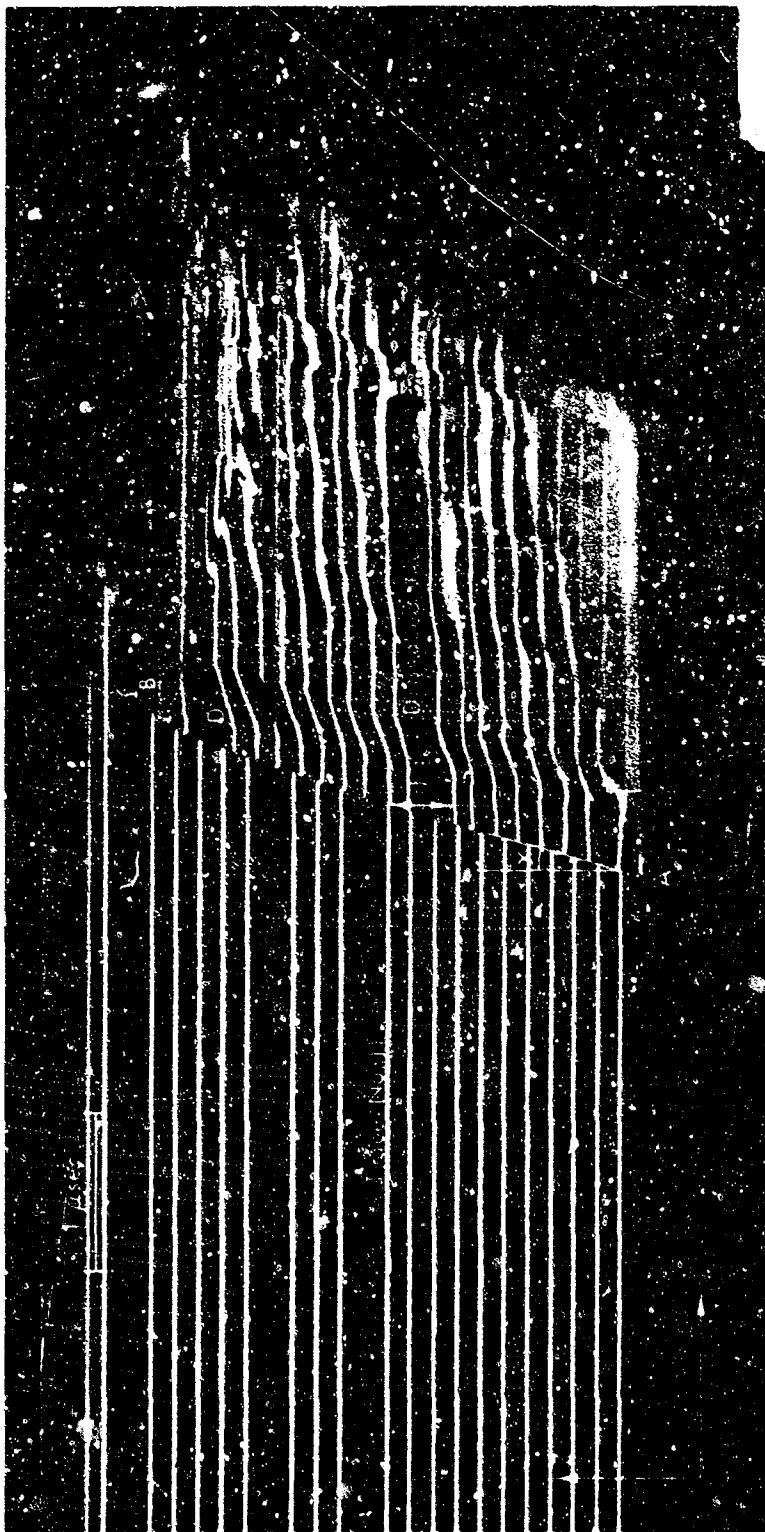
FIG. 11 STREAK CAMERA RECORD FOR SHOT 11,190 (Line AB indicates the position of the shock-foil intersection. Line CD indicates the presence of a rarefaction wave. J is the jump as recorded on film, $x - J/R_0$.)

The peak shock pressure in the driver can be inferred with the use of the cell if the wave is not attenuating. The peak pressure in the fluid is calculated using measurements obtained in the fluid, and the corresponding peak shock pressure in the driver is determined by impedance matching. However, if the shock wave is not flat-topped, the pressure measured at the foil will in general not be representative of the peak pressure in the driver, since the peak pressure changes as the front propagates through the liquid.

Analysis of the inclined foil record gives the pressure at the several locations of the jumped grid lines. Since the foil is inclined with respect to the direction of shock propagation, the peak shock pressure as a function of depth is obtained. With the use of large foils or double foils (i.e., two foils per cell) the peak pressure can be measured over considerable depth in the liquid. This information is relevant to the attenuation characteristics of the fluid.

In Fig. 11 it can be noted that the grid traces are visible after they have jumped. Since the foil moves with the fluid velocity, the motion of the displaced grid lines should indicate the motion of the fluid after the shock front has passed over the foil. In principle, the gage is then capable of providing information not only about the peak shock pressure but also about a portion of the relief. This type of information--i.e., pulse shape in the liquid as a function of time and depth--can then serve as a check of computer calculations of the shock flow in the fluid and in the metal cell bottom.

The refractive index is known to depend on the density and, less importantly, on the temperature of a liquid. The gage can be employed to determine the refractive index of shocked liquids. In fact, a knowledge of the refractive index is necessary before any of the shock flow parameters can be obtained with this device.

The liquid cell can also be designed so that disturbances overtaking the shock from the rear can be observed with the inclined foil arrangement. The propagation of shocks or relief waves is indicated by additional motions of the displaced traces. In the case of overtaking shocks, the grid lines jump a second time as the shock passes over the foil, and the motion of the second shock front is indicated by another slant line on the film.

Figure 11 is a record obtained when a rarefaction moves over the foil after the initial shock front passage. The grid lines are displaced back towards their original position, along the line CD, indicating a decrease in particle velocity. Reduction of such foil data yields the relief wave velocity and the change in the particle velocity.

Consider, for example, the measurement of the relief wave velocity in the driver using this technique. Let the shock in the driver be produced with a flying plate of the same material. The shock propagates into the driver and then into the liquid cell where foil motion is observed. The backward-facing shock produced at impact is reflected at the rear of the flyer plate and becomes a forward-facing rarefaction fan. Figure 12 is a time-distance diagram illustrating the wave trajectories. The thickness of the cell bottom or driver, the foil angle, and depth are chosen so that the head of the rarefaction wave will overtake the forward-facing shock front when it is still interacting with the foil. Measuring the depth at which the relief wave overtakes the shock locates the point P in Fig. 12. The foil analysis gives the particle velocity, sound speed, and shock velocity in the fluid so that segments OP, OS, and SP can be drawn. The points A and B can be located with a knowledge of the shock velocity in the driver. The minimum relief wave velocity is now just the slope of a straight line segment from B to O. The absolute magnitude can be computed only if the sound velocity in the driver is known in the triangular region COS. By using thicker cell bottoms, the error in
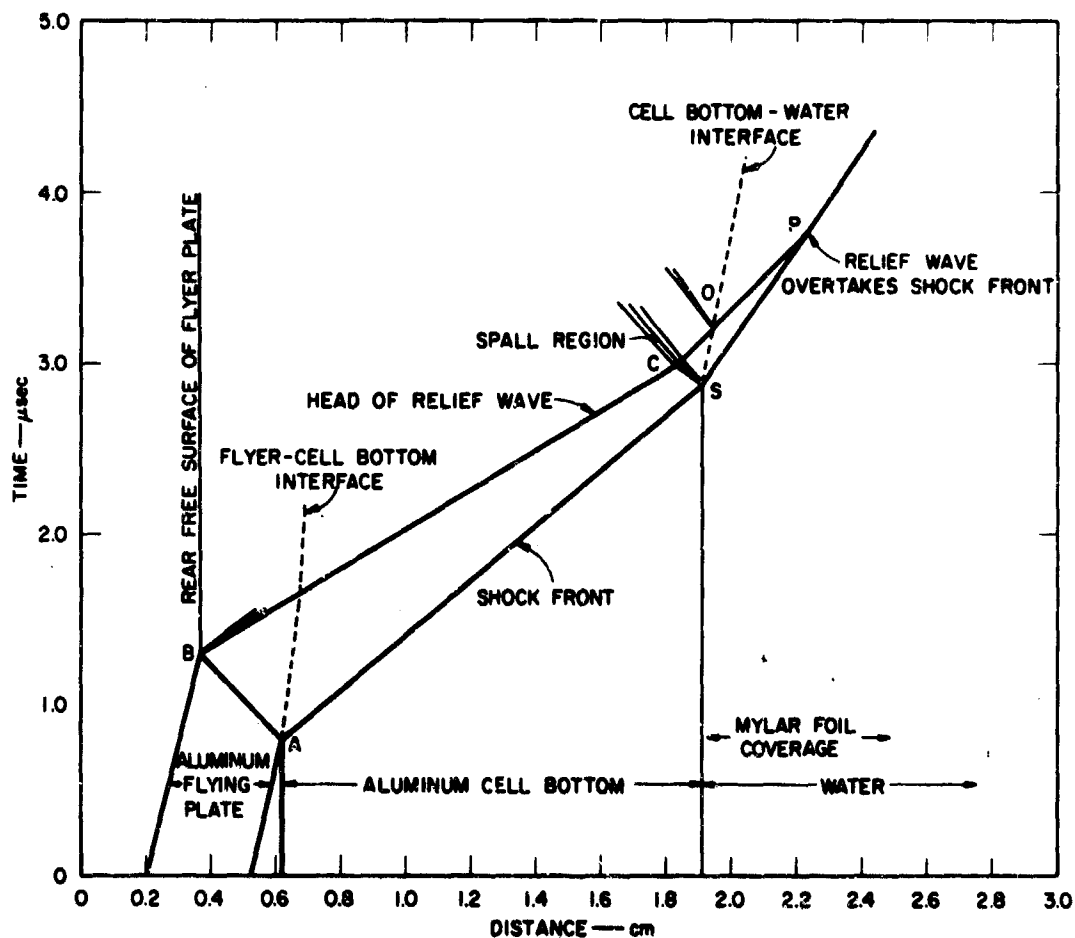
FIG. 12 TIME-DISTANCE DIAGRAM ILLUSTRATING THE WAVE TRAJECTORIES
IN SHOT 11,762

the initial elastic sound speed due to the uncertainty in the sound veloc-
ity along segment CO can be reduced. However, since the elastic relief
wave must be observed in the fluid cell before overtaking the shock front,
a maximum driver thickness exists.

Several problems have been encountered in the application of
the immersed foil gage. First, the use of an evacuated region between
the flyer and driver results in bowing of the driver somewhat, depend-
ing on its construction. The result is that, upon flying plate impact, a
nonplanar shock is produced in the driver. Since the analysis is one-
dimensional, such a three-dimensional shockwave is undesirable.

31

Another problem exists when studying attenuation shocks with a gage made of a material of lower shock impedance than the specimen to which the gage is attached. The interaction of the rarefaction fan that that is reflected back into the specimen at the specimen-liquid interface (CS in Fig. 12) and the forward facing rarefactions in the attenuating input wave may cause the specimen to spall. Therefore, the useful observation time of the initial wave in the fluid cell is limited by the arrival of the spall signal.

b. Results

Water was used in the immersed foil gage experiments performed on this project because of the amount of equation of state data available. The gages were mounted as shown in Fig. 10 for the flying plate experiments. The cell bottom was either annealed or hardened 2024 aluminum. The flying plate assemblies were similar to the ones used for the low velocity attenuation experiments.

Two experiments were conducted where the annealed aluminum cell bottoms were 0.080-inch thick and the aluminum flying plates were also 0.080-inch thick. The plates reached a velocity of 0.133 cm/μsec. Figure 11 is an example of the photographic record obtained. The shock wave that intersected the immersed foil in this shot was flat-topped, i.e., the reflected relief had not yet overtaken the shock front. The locus of trace end-points, line AB, would be a straight line if the shock velocity were constant and the wave were plane. However, due to the bowing of the cell bottom when the flying plate chamber was evacuated, the center of the cell base was impacted by the flyer before the edges and a curved shock front propagated into the water. The curved line from A to B is the result of this nonplanar shock.

Notice that the traces along the line CD began to move toward their original position. This trace motion indicates the propagation of

32

a rarefaction wave through the water. It relieved the pressure rapidly
at first and then more slowly. The initial decrease in fluid particle
velocity corresponded to the arrival of the relief wave originating when
the left-facing shock in the flyer reflected from the rear of the flying
plate.

It was hoped that the trace records after jump would yield more
information on the shock profile as a function of time. However, due to
the uncertainties caused by the curved shock and the indefinite motion
of the traces, the additional pulse shape information has not yet been
deduced from the data. Calculations based on this experimental
arrangement indicate that the cell bottom will spall. The recording
times in the experiment were long enough to observe the spall signal
but it has not been identified.

Shot 11,253 involved the use of a water gage in which two reflect-
ing Mylar foils were mounted one above the other. The 1/8-inch flying
plate impacted a 1/8-inch annealed 2024 aluminum cell bottom at 0.127
cm/μsec. The additional bottom thickness somewhat reduced the curva-
ture of the shock front. The record also indicates the motion of the re-
lief waves into the cell. The depth at which the relief overtook the
shock front was 0.313 inch in the water.

As discussed earlier, a measurement of the relief wave velocity
in the aluminum cell bottom can be made more precisely if the cell
bottom is thicker but not so thick that the relief wave BC overtakes the
shock front in the aluminum rather than in the water. Shot 11,762 was
conducted in order to measure the initial relief wave velocity in 2024-
T351 aluminum. Figure 12 is the corresponding time-distance diagram.
The 1/8-inch flying plate acquired a velocity 0.128 ± 0.02 cm/μsec
and impacted the 0.507-inch-thick aluminum cell bottom. Calculations
based on the experimental results indicate a minimum initial relief

33

wave velocity at 110 kbars in the aluminum of 0.77 cm/μsec. The actual velocity must be greater than this because the sound speed in the region COS, which is already somewhat relieved, is less than the initial relief wave velocity in the fully stressed material.

A calculation was performed using the constant Poisson's ratio elastoplastic theory to determine the sound speed in the region COS of Fig. 12. It was assumed that the head of the relief disturbance moved through a uniform region along OC where the stress was 35 kbars. The resulting sound speed was 0.553 cm/μsec. Employing this value to calculate the elastic sound speed along BC gave $c_{el} = 0.81$ cm/μsec, which is in excellent agreement with the 0.80 cm/μsec obtained by measuring the free-surface velocity of aluminum samples as described later.

SECTION IV

EXPERIMENTAL RESULTS

1. Aluminum (Low Velocity Flyer Plates)

Results of experiments in which both the flyer plates and the target plates were as-received 2024-T351 aluminum are shown in Fig. 13, where half the free-surface velocity is shown as a function of the thickness of the target. The data are plotted in this way to facilitate comparison with calculated results. Target thicknesses are given in multiples
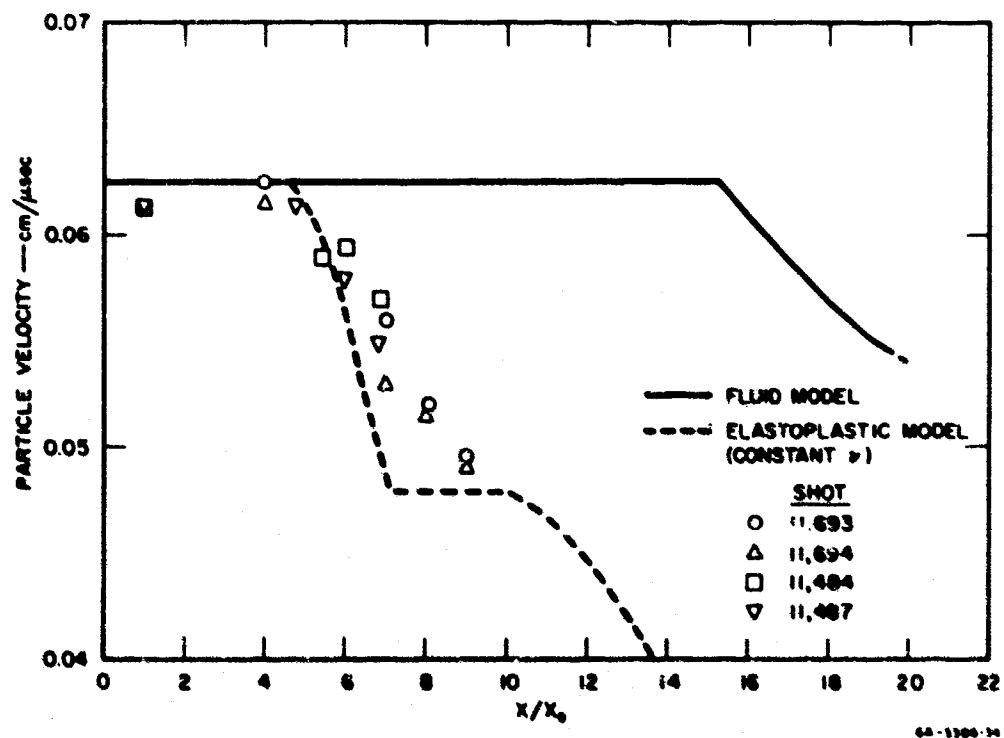
FIG. 13 PEAK PARTICLE VELOCITY vs. SHOCK TRAVEL (x/x_0) FOR 2024-T351 ALUMINUM IMPACTED AT 0.125 cm/µsec

of the flyer plate thickness, x_o, which for the experiments reported here was 0.125 inch. Two separate experiments gave particle velocities of 0.0615 cm/µsec for $x/x_o = 1$, i.e., the free-surface velocity

35

was 0.123 cm/μsec when the targets were 0.125-inch thick. This agrees well with the flyer plate velocity, which ranged from 0.124 to 0.126 cm/μsec.

Comparison of the experimental and calculated results shows that the two agree fairly well as to the point at which attenuation begins, approximately 5.5 plate thicknesses. Closer agreement can be obtained by using a smaller increment in the calculations. For the results presented here, 20 increments were used for each plate thickness (0.32 cm). The curve for the computed results shows a flat portion at seven to nine plate thicknesses. The experimental results show no tendency for the curve to become flat. This continuous decrease of the particle velocity in the experimental results forces a revision of the stress-strain relations used in the computational model.

Results obtained previous to this project for 2024-T4 annealed aluminum are given in Fig. 14 along with the results shown in Fig. 13. Results of Shot 10,227 agree well with the new data, while those of Shot 10,354 do not. It is probable that the flying plate velocity was somewhat higher in Shot 10,354 than in Shot 10,227 and the plate velocity experiments.[7]

However, the results at eight and nine plate thicknesses for Shot 10,354 show that the decay rate of peak pressure with distance was almost zero, as was also observed in earlier experiments.[3] Preference in this situation is given to the new data which give nc evidence of a plateau. The comparison indicates that annealing 2024 aluminum makes no measurable difference in the target thickness at which attenuation commences. The difference in behavior at eight and nine plate thicknesses could possibly be due to the use of annealed aluminum in the

36
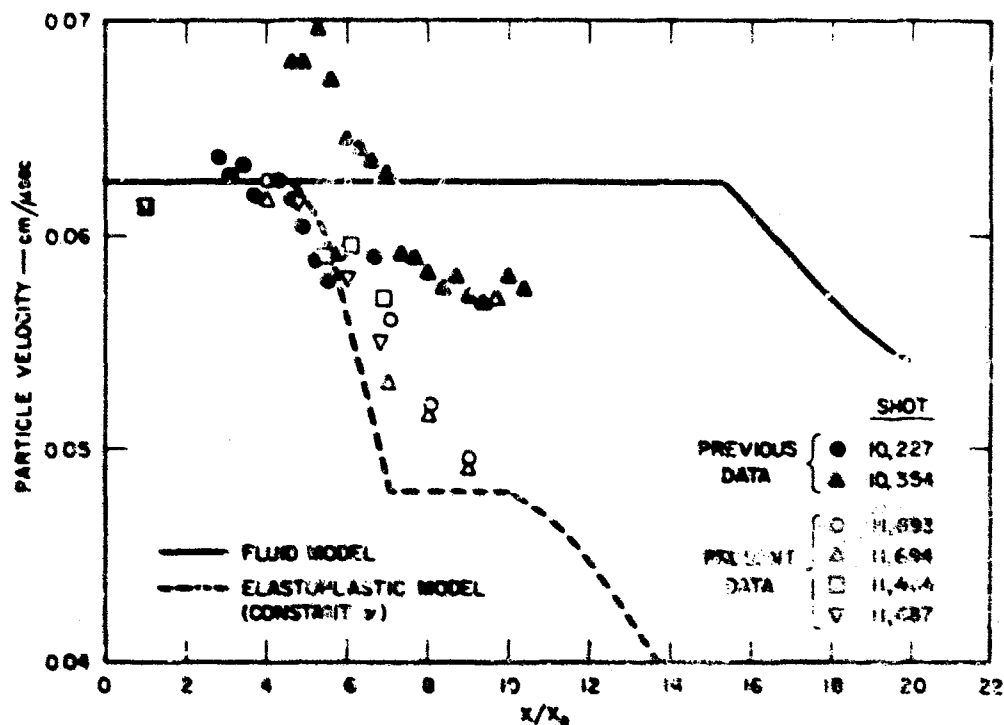
FIG. 14 PEAK PARTICLE VELOCITY vs. SHOCK TRAVEL (x/x_0) FOR 2024-T35!
ALUMINUM AND 2024 ANNEALED ALUMINUM IMPACTED AT 0.125 cm/μsec
(Shots 10,227 and 10,354 were reported previously for the annealed aluminum)

earlier study or to the use of different techniques for measuring the free-surface velocity.

Results of attenuation experiments using annealed 1060 aluminum are given in Fig. 15 for both the current and the earlier shots. If the point for which $x/x_0 = 1$ and the particle velocity of 0.0685 is ignored, the average particle velocity in the absence of attenuation was about 0.0635 cm/μsec (using only the new data). That is, the average shim velocity was about 0.127 cm/μsec. The velocity of the 1060 projectile plate was about 0.126 ± 0.001 cm/μsec for these new experiments. Hence the higher particle velocity for thin 1060 aluminum targets as compared with 2024 targets (Figs. 13 and 14) is at least partly due to the fact that the 1060 flyer plates acquired greater velocity than did the 2024 flyer plates. Attenuation starts at about six plate thicknesses in 1060 aluminum.
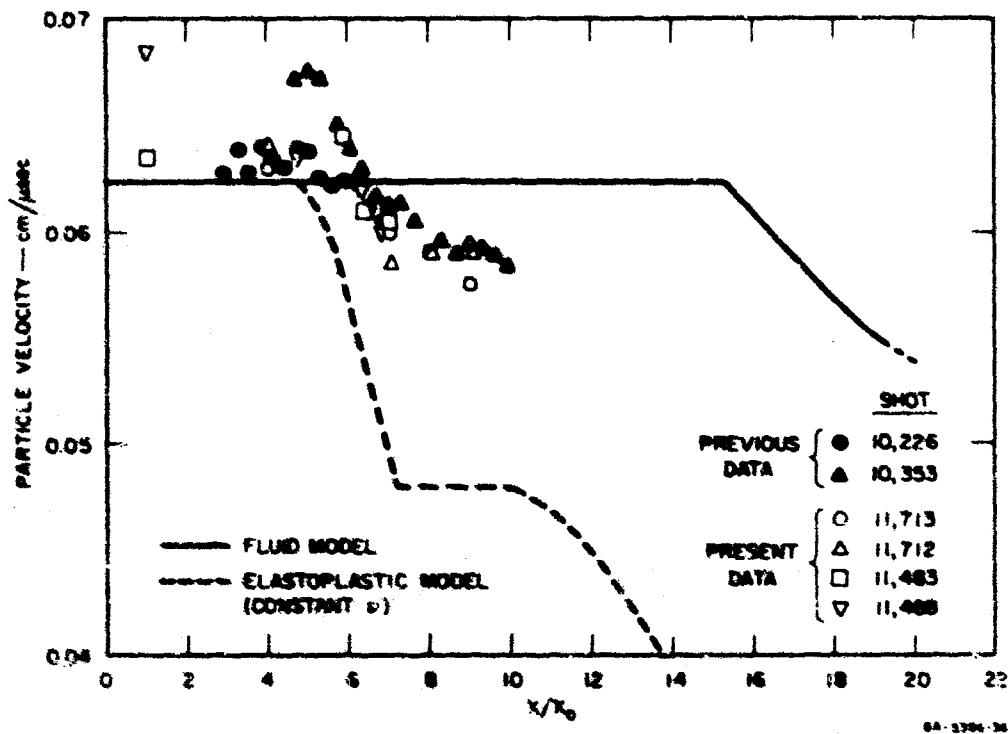
FIG. 15 PEAK PARTICLE VELOCITY vs. SHOCK TRAVEL (x/x_0) FOR 1060 ANNEALED ALUMINUM IMPACTED AT 0.125 cm/μsec

The results of the new study of 1060 aluminum shows some indication of a flat region at seven and eight plate thicknesses similar to the flat part of the calculated curve. The same trend is evident in the results of the earlier Shot 10,353, which had a higher flying plate velocity than Shot 10,226.

The value of the stress relief provided by the elastic wave, $(\sigma_e - \sigma_f)$ in Section II, is not obtainable from the data for either 1060 or 2024 aluminum in a reliable way. As shown in Section II, the value of $(\sigma_e - \sigma_f)$ is necessary for a determination of the yield strength when the elastoplastic equation of state is assumed. Figure 14 gives an indication that the decrease in particle velocity may be about 0.009 cm/μsec, corresponding to a drop in peak shock strength of 25 kbars. The data for

38

the 1060 aluminum give a more definite indication of a plateau in the plot and hence a more reliable value of the decrease in stress $(\sigma_e - \sigma_f)$. The value appears to be 10 kbars.

Table III gives the complete results for all attenuation experiments performed during the current program. The data for the low velocity plate slap experiments on aluminum as well as the high velocity experiments with Teflon and aluminum are presented.

2. 2024-T351 Aluminum (High Velocity Flyer Plates)

Two experiments were performed with 2024-T351 aluminum in the as-received condition for which the flyer plate velocity was about 0.32 cm/μsec. This velocity corresponds to a pressure of about 345 kbars in aluminum. Results of the shots are given in Fig. 16 along with the calculated curves using a fluid-type equation of state and the constant Poisson's ratio elastoplastic model. The average shim velocity in Shot 11,824 for specimen thicknesses out to 4.1 plate thicknesses is 0.324 cm/μsec. The projectile velocity for the shot was 0.316 ± 0.005 cm/μsec. Hence the free-surface velocity appears to be slightly greater than the velocity of the flyer plate. The calculations were done using a velocity of 0.33 cm/μsec. Shot 11,861 shows that the particle velocity has been reduced below that predicted by the fluid model, but not as much as predicted by the elastoplastic model. The attenuation started between 4.1 and 5.2 plate thicknesses, implying a sound speed of about 0.93 cm/μsec behind the shock front. The data indicate that the attenuation of stress is about 65 kbars, and there is no assurance that this is due entirely to the elastic wave.

3. Pressure Dependence of Shear Modulus and Yield Stress of 2024-T351 Aluminum

The speed of the head of the elastic relief wave can be determined by locating the point at which it overtakes the shock front, point M in

Table III

FLYING PLATE ATTENUATION MEASUREMENTS

Material	Initial Condition	Shot Number	Low Velocity			
			Flying Plate Velocity (cm/μsec)	Flying Plate Thickness x_0 (cm)	Sample Thickness (x/x_0)	Free-Surface Velocity (cm/μsec)
1060 aluminum	Annealed	11,483	0.127 ± .002	0.3124	1.02	0.127 ± .002
					5.84	0.129 ± .002
					6.37	0.122 ± .002
					6.99	0.121 ± .002
		11,488	0.125 ± .003	0.3175	1.01	0.137 ± .004
					4.76	0.127 ± .002
					6.31	0.124 ± .001
					6.83	0.120 ± .001
		11,712	0.129 ± .002	0.3162	4.02	0.128 ± .001
					7.05	0.117 ± .001
					8.05	0.118 ± .002
					9.05	0.118 ± .001
		11,713	0.128 ± .002	0.3175	4.00	0.126 ± .002
					6.99	0.120 ± .001
					8.00	0.118 ± .001
					8.99	0.115 ± .001

Table III (continued)

Material	Initial Condition	Shot Number	Low Velocity			
			Flying Plate Velocity (cm/μsec)	Flying Plate Thickness x_o (cm)	Sample Thickness (x/x_o)	Free-Surface Velocity (cm/μsec)
2024-T351 aluminum	As received	11,484	0.128 ± .005	0.3150	1.01	0.123 ± .002
					5.45	0.118 ± .003
					6.06	0.119 ± .063
					6.90	0.114 ± .002
		11,487	0.128 ± .003	0.3175	1.00	0.123 ± .001
					4.77	0.123 ± .001
					6.00	0.116 ± .003
					6.83	0.110 ± .002
		11,693	0.127 ± .002	0.3150	4.01	0.125 ± .001
					7.05	0.112 ± .002
					8.08	0.104 ± .001
					9.02	0.099 ± .001
		11,694	0.128 ± .003	0.3175	4.01	0.123 ± .001
					7.00	0.106 ± .002
					8.00	0.103 ± .001
					9.00	0.098 ± .003
	Annealed	11,762	0.130 ± .002	0.3175	4.06	0.125 ± .001
		11,414	0.126 ± .001	0.3175	1.00	0.126 ± .001

Table III (concluded)

Material	Initial Condition	Shot Number	Flying Plate Velocity (cm/μsec)	High Velocity		
				Flying Plate Thickness x_0 (cm)	Sample Thickness (x/x_0)	Free-Surface Velocity (cm/μsec)
2024-T351 aluminum	As received	11,824	0.320 ± .005	0.3073	2.07	0.325 ± .009
					3.10	0.322 ± .003
					4.13	0.327 ± .001
					5.16	0.300 ± .009
		11,861	0.324 ± .005	0.3099	2.04	0.326 ± .003
					3.59	0.318 ± .009
					7.18	0.281 ± .005
					8.19	0.272 ± .007
Teflon*		11,864	0.315 ± .010	0.3099†	2.07	0.439 ± .004
					4.11	0.309 ± .003
					6.13	0.211 ± .002
					8.21	0.183 ± .002

* Manufactured by AVCO.
† Aluminum flyer.
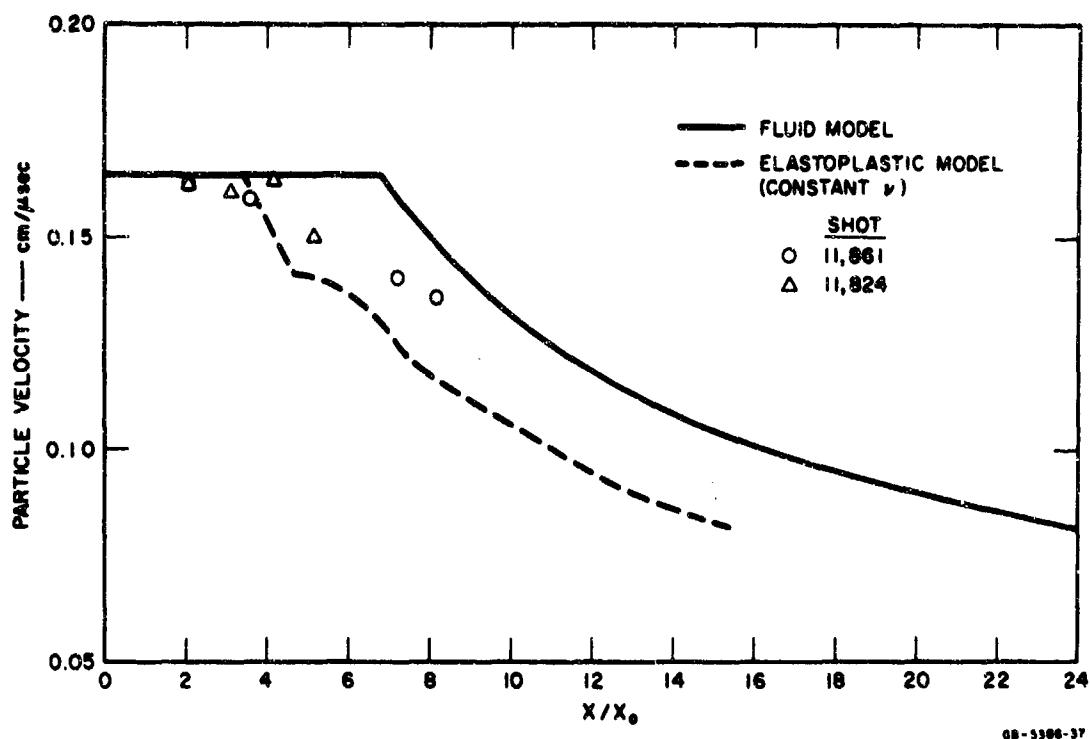
FIG. 16   PEAK PARTICLE VELOCITY vs. SHOCK TRAVEL (x/x_0) FOR 2024–T351
ALUMINUM IMPACTED AT 0.33 cm/μsec

Fig. 2.[12] This point corresponds to the target thickness at which the
peak particle velocity first begins to drop, as shown in Figs. 13 through
16.   There are other methods for determining the relief wave velocity.
Al'tshuler et al.[16] describe a "lateral-relaxation" method and an
"overtaking-relaxation" method, the latter being similar to the tech-
nique described above.   Still another is based on the analysis of the
fluid gage records (Section III-3).   Both the overtake and fluid gage
methods were used in the experiments in which the lower velocity plates
impacted 2024 aluminum targets.   Fluid gages were not used with
higher velocity plates or with 1060 aluminum targets.

   From the measured elastic wave speeds and associated free-
surface velocities, together with independent Hugoniot equation of state
measurements, values of the elastic shear modulus, G, can be derived

43

as shown in Section II. These values and other quantities derived from the experiments are listed in Table IV.

The elastoplastic model as currently formulated predicts an initial separation of the elastic and plastic relief waves with a relatively constant region between them. This separation should show up as a step in the decay curve as indicated by the theoretical curves of Figs. 13 through 16. The drop in particle velocity to the step is a measure of the yield strength of the shocked state. The data, however, do not clearly show such a step except possibly for 1060 aluminum (Fig. 15), and one shot (No. 10,354) on annealed 2024-T351 aluminum (Fig. 14). Consequently, values for the yield strength [more exactly $(\sigma_e - \sigma_f)$] that are clearly reliable cannot be directly obtained.

It should be noted, however, that within the context of the theoretical model assumed, all parameters except the yield strength are determined directly from experiment (including G). Consequently, to the extent that the model is correct an effective value for Y can be deduced by trial and error by requiring agreement between the calculated and the measured decay curves.

Values of G and $(Y_e + Y_f)$ determined from the experiments are shown as functions of the specific volume in Fig. 17. The zero stress value of G, 0.287 Mbar, and the approximate value of Y_0, 0.0025 Mbar, are also shown in the figure. The possible errors in the data at the high stress point are so large that no conclusive inferences can be drawn about functional relationships. However, several relationships can be assumed that are consistent with the data; these permit calculations of shock decay to be made that can be usefully compared with experimental attenuation data.

The functions chosen for an initial trial comparison of theory and experiment are the curves labeled I in Fig. 17. The shear modulus

44

Table IV

VALUES OF EXPERIMENTAL PARAMETERS
FOR 2024-T351 ALUMINUM

Parameters	Flyer Plate Velocity (cm/μsec)	
	0.125	0.33
Peak stress (Mbars)	0.110	0.345
Sound speed, c(cm/μsec)*	0.80 ± 0.02	0.93 ± 0.05
Sound speed, c(cm/μsec)†	0.81	--
G (Mbars)	0.54 ± 0.07	0.59 ± 0.25
K (Mbars)	1.27	2.28
$\sigma_e - \sigma_f$ (Mbars)	0.025	0.065
$Y_e + Y_f$ (Mbars)	0.013 ± 0.008	0.025 ± 0.008
Coordinate of point M, Fig. 2	5.5	4.5
Flyer plate thicknesses (cm)	0.32(nominal)	0.32(nominal)

* Aluminum free-surface velocity vs depth measurements.
† Immersed foil water gage measurement.
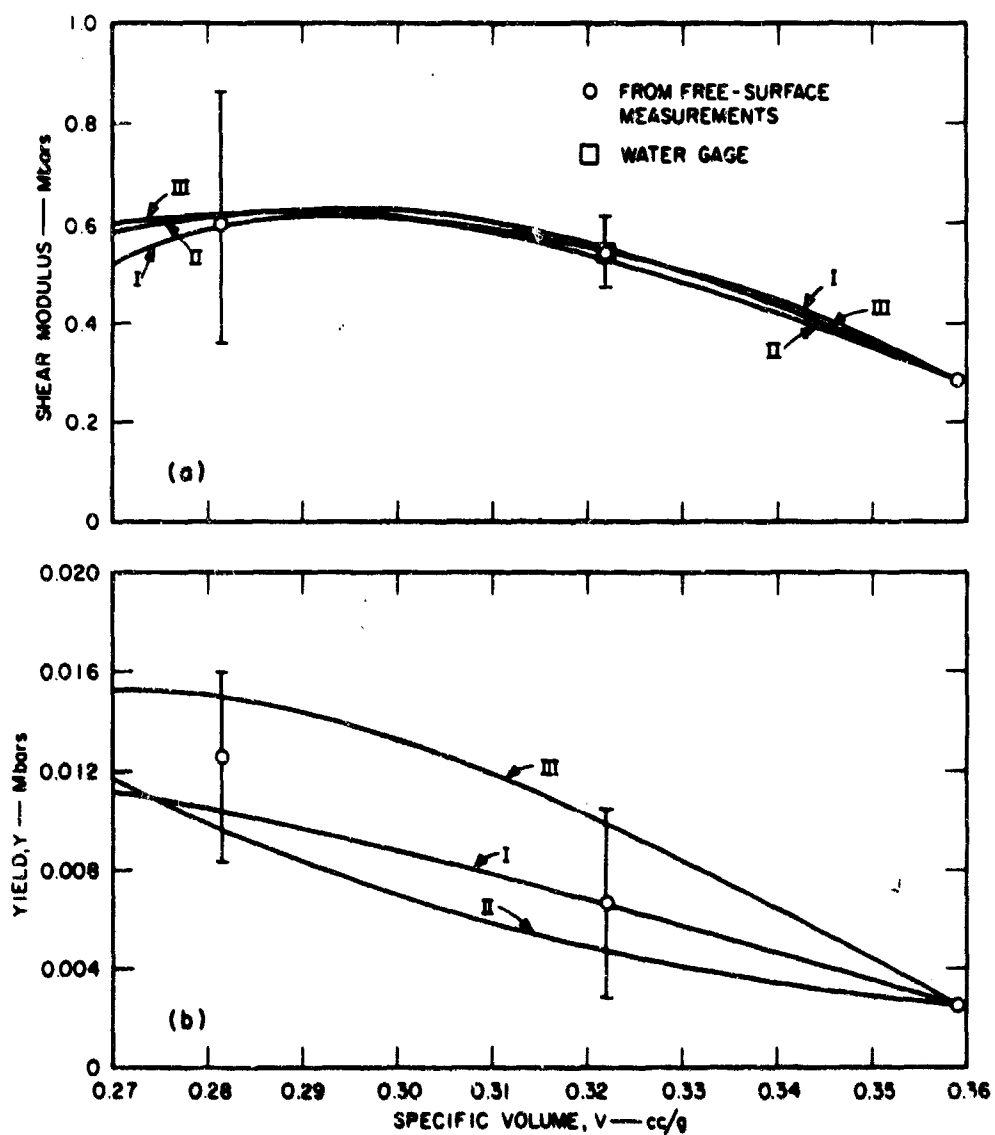
FIG. 17 SHEAR MODULUS, G, AND YIELD STRESS, Y, vs SPECIFIC VOLUME, V

is specified by (Fig. 17a)

$$G = 0.287 + 2.99\mu - 6.88\mu^2 \qquad (20)$$

where $\mu = V_0/V - 1$ and the yield strength by (Fig. 17b)

$$Y = 0.0025 + 0.0407\mu - 0.0432\mu^2 \qquad (21)$$

The hydrostat is then given by

$$P = 0.764\mu + 1.37\mu^2 + 1.103\mu^3 \tag{21}$$

The curves labeled II and III are modifications of the above equations chosen in an attempt to improve the fit over that given by curves I. These are primarily alternative functions for the yield strength, since it is subject to the largest experimental uncertainty. A weak coupling between the shear modulus and the yield strength exists for a given hydrostat; this coupling is the source of the differences in curves I, II, and III of Fig. 17a.

Note that the functions for G exhibit a maximum value near $\mu = 0.217$ (V = 0.295 cc/g). The corresponding pressure is about 250 kbar. It would be of considerable interest to better determine experimentally whether the shear modulus possesses such a maximum along the Hugoniot curve, since this would indicate a trend toward true fluid behavior.

4.   Flow Calculations for 2024-T351 Aluminum

Results of flow calculations using the assumptions mentioned above are given in Fig. 18 for the lower velocity impact case, and in Fig. 19 for the higher velocity case. The a, b, and c portions of each figure refer to the fits designated as I, II, and III of the preceding section.

For lower impact velocities, fit I (Fig. 18a) shows reasonable agreement but exhibits a stepwise decrease in particle velocity that is not evident in the data. At higher velocities (Fig. 19a) this fit compares favorably at five plate thicknesses but falls off too quickly thereafter.

Fit II shows less of a step in the decay curve for lower velocity impact, but falls off too slowly at the greater target thicknesses (Fig. 18b). The agreement for higher impact velocity is quite good (Fig. 19b).

47

FIG. 18 COMPARISON OF EXPERIMENTAL
AND CALCULATED RESULTS,
2024-T351 ALUMINUM IMPACTED
AT 0.125 cm/μsec

FIG. 19 COMPARISON OF EXPERIMENTAL
AND CALCULATED RESULTS,
2024-T351 ALUMINUM IMPACTED
AT 0.33 cm/μsec
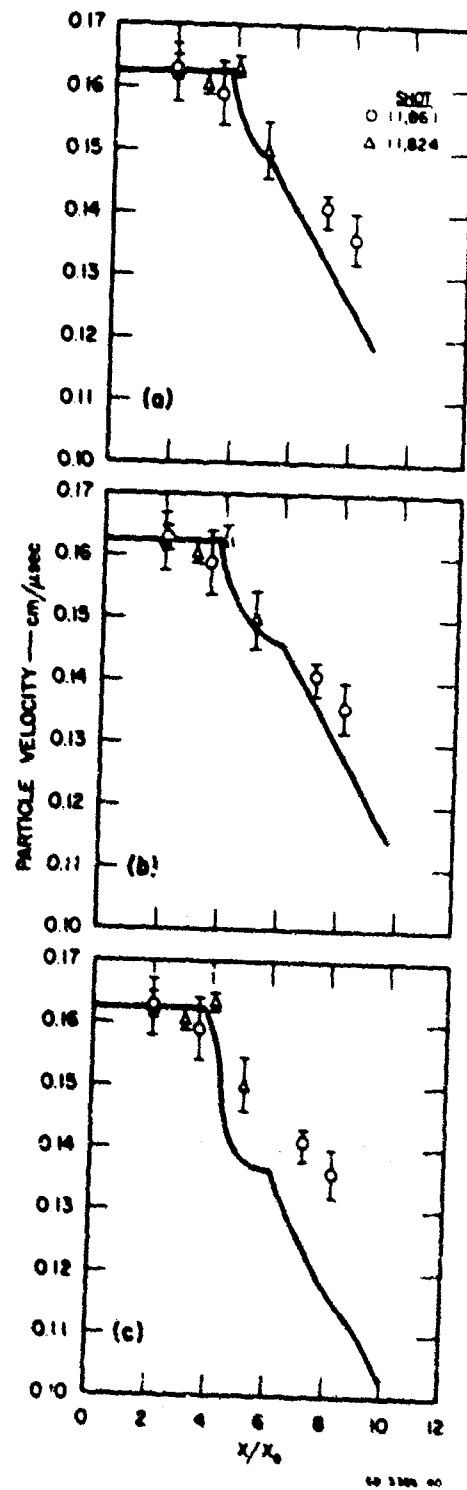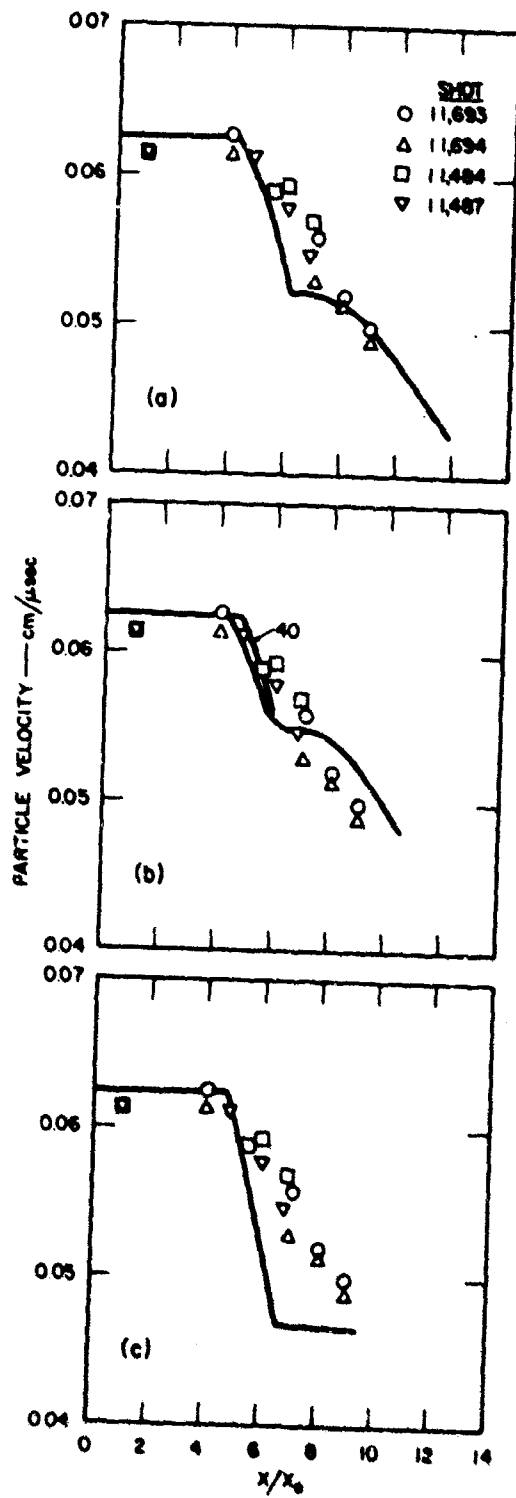
The effect of increasing the number of cells in the calculations is shown by the curve labeled "40" in Fig. 18b. In this calculation the flyer plate was zoned to contain 40 cells rather than 20 as used in all the other calculations. It may be noted that the elastic sound speed (0.8 cm/μsec, Table IV) was determined by using the experimental value of 5.5 plate thicknesses for the depth at which the rarefaction overtakes the shock front. Zoning the flyer plate with only 20 cells places the apparent point of overtaking at $x/x_o = 4.5$; with 40 cells this point moves to $x/x_o = 5.0$. Presumably, convergence to the value 5.5 would occur with increasingly fine zoning.

The fit shown as curve III in Fig. 17 clearly gives the least satisfactory fit to the decay curves, as shown in Figs. 18c and 19c.

The results of these attempts to fit the decay curves indicate that the elastoplastic theory as formulated is probably oversimplified. No step in the decay curves can be clearly identified, at least for 2024-T351 aluminum. This implies that there is no pronounced separation of the elastic and plastic rarefaction waves.

The most likely explanation for this difference is that a Bauschinger effect tends to spread the elastic rarefaction so that it merges with the following plastic wave. Bauschinger effects have been observed in plane shock waves at much lower pressures.[3,4]

5.   Teflon

The attenuation experiments on Teflon* were conducted using thin (0.0008-inch) aluminized Teflon shims to measure the initial free-surface velocity. The samples were arranged in the same manner as

---

* Teflon manufactured by AVCO Corporation, Wilmington, Mass. Mean density, 2.195 g/cc.

49

the aluminum samples described in Section III and were impacted by a
1/8-inch aluminum flying plate. The photographic record for Shot
11,864 is shown in Fig. 20.

The four Teflon samples were of different thicknesses, corres-
ponding to multiples of flyer plate thicknesses of 2.1, 4.1, 6.1, and
8.2. In Fig. 20, the line AA represents the time at which the shim
first moved. Line BB indicates the shim arrival at the cover glass
after having crossed a 0.48-cm gap. The third event at CC is inter-
preted as the arrival of the surface of the Teflon sample as was done
earlier for aluminum (Fig. 9). The presence of the second arrival
indicates that the Teflon also had a tensile strength after being shocked.

The results of the free-surface velocity measurements appear in
Table III. The flying plate velocity was 0.315 ± 0.010 cm/μsec. A
graphical impedance solution indicated that the peak induced particle
velocity in the Teflon was 0.198 ± 0.005 cm/μsec. The corresponding
pressure was 220 kbars.[17]

Note that the thinnest sample was only two flyer plate thicknesses.
The free-surface velocity measured at this depth was 0.439 ± 0.004
cm/μsec. This may or may not represent the peak stress in the Teflon,
for there is no assurance that the shock front had not begun to attenu-
ate by $2x_c$. However, a time-distance diagram shows that the rare-
faction wave from the rear of the flyer plate would have had to have an
almost infinite velocity in order to overtake the shock front by $1\frac{1}{2}x_0$.
A more reasonable rarefaction wave velocity predicts the initial attenu-
ation to occur somewhat deeper than $2x_0$.

Considering free-surface velocity of the thinnest sample to repre-
sent the amplitude of the unattenuated incident shock, it is seen at once
that the free-surface approximation, i.e., $u_p = \frac{1}{2}u_{fs}$, is a poor one in
this experiment. One half of u_{fs} is 0.22 cm/μsec, whereas the induced
particle velocity was 0.198 cm/μsec

50
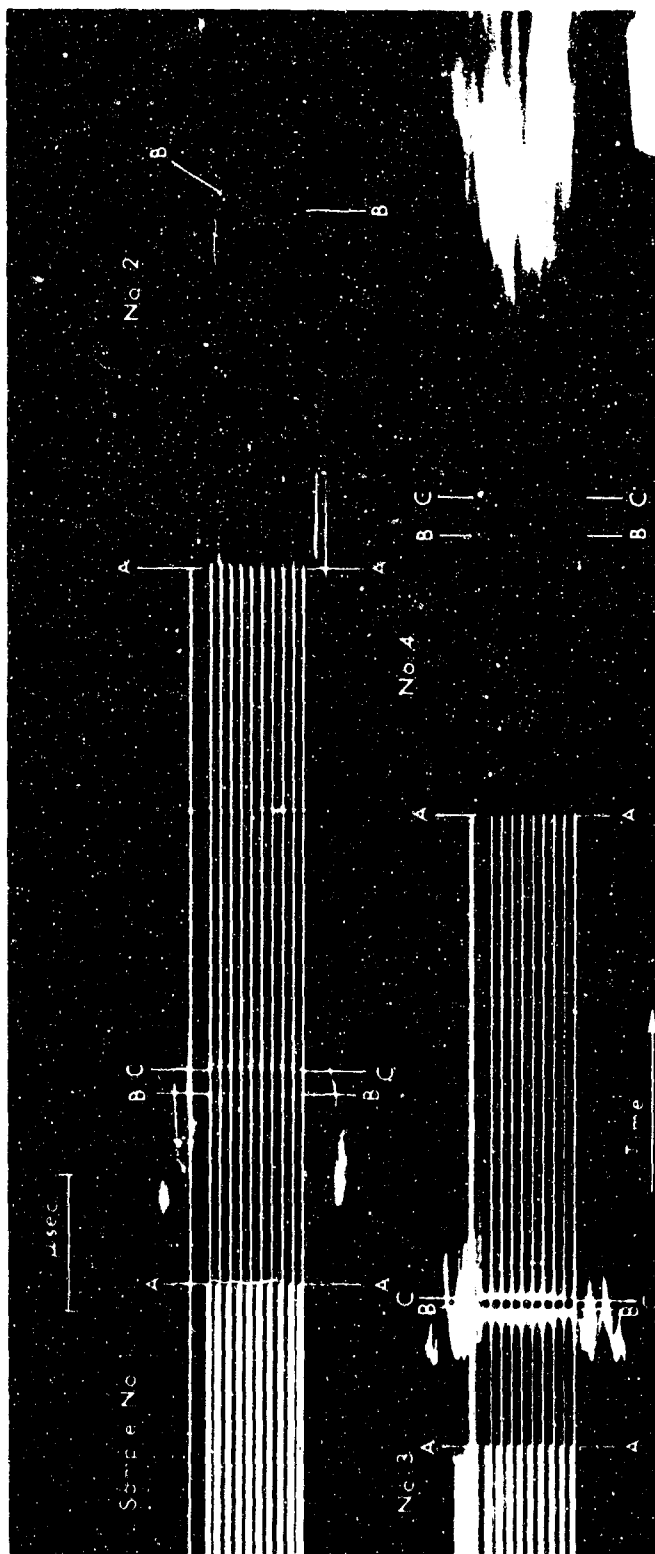
FIG. 20 STREAK CAMERA RECORD, SHOT 11,864, ALUMINUM FLYING PLATE IMPACTING TEFLON. Sample thickness is multiples of flyer plate thickness x_0. Sample No. 1 — 4.1 x_0, Sample No. 2 — 8.2 x_0, Sample No. 3 — 2.1 x_0, Sample No. 4 — 6.1 x_0, (x_0 = 0.3099 cm)

51

A computer calculation was performed for a 1/8-inch aluminum plate impacting Teflon at 0.32 cm/μsec. The results of this calculation are shown in Fig. 21. The constant Poisson's ratio equation of state for aluminum was used with M = 0.055 (see Section II). The Teflon Hugoniot was represented by

$$P_H = 0.112\,\mu + 0.491\,\mu^2 + 0.248\,\mu^3 \,, \tag{22}$$

the data being obtained from Netherwood.[18]
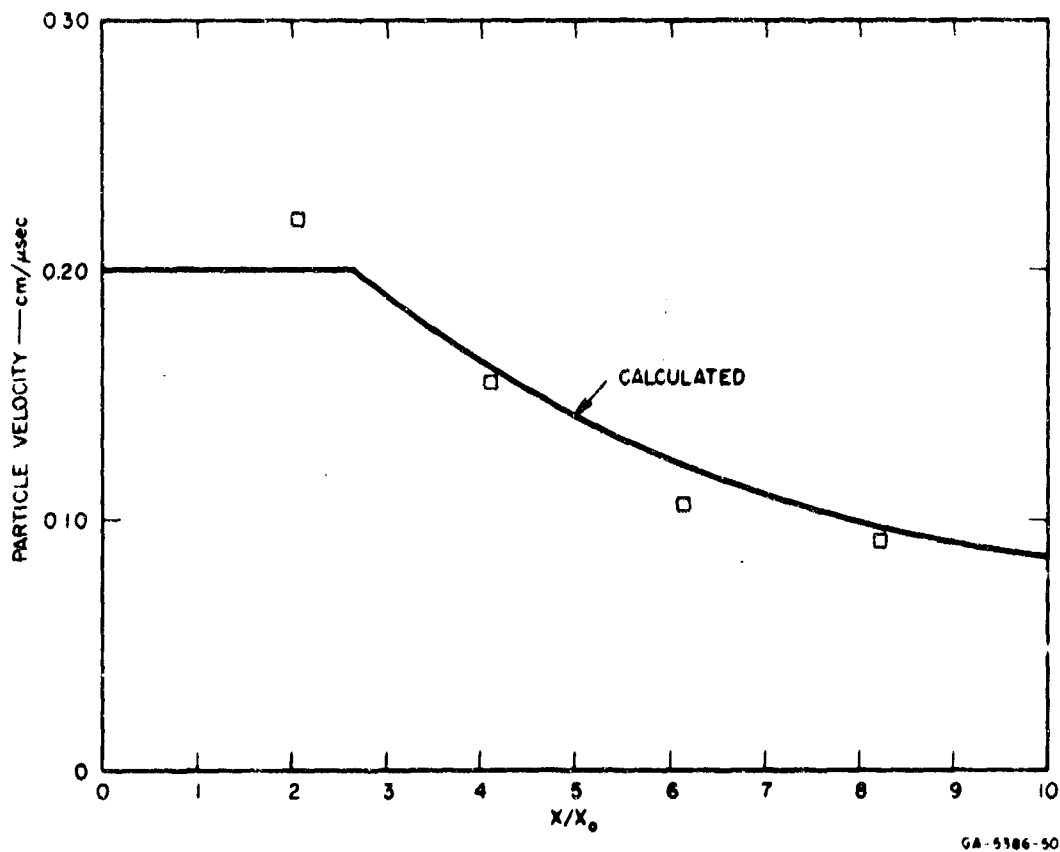
FIG. 21 CALCULATED AND EXPERIMENTAL RESULTS FOR 0.31-cm ALUMINUM PLATE IMPACTING TEFLON (Experimental values are 1/2 u_{fs} as measured in Shot 11,864)

52

The sound speed in the Teflon was then obtained from

$$c = \sqrt{dP_H/d\rho} \qquad (23)$$

where P_H is the pressure along the Hugoniot.

The experimental points plotted in Fig. 21 are one-half the measured free-surface velocities. These show strikingly good agreement with the theoretical curve, but to some extent the agreement is fortuitous because the free-surface approximation is inaccurate. Nevertheless, no pronounced elastoplastic effects are evident and it appears that the fluid model may be adequate. More information on the complete P-V-E equation of state for Teflon would permit a more critical evaluation of the fluid model to be made.

SECTION V

CONCLUSIONS

Shock wave attenuation data are presented for aluminum of types 2024-T351 and 1060, and for Teflon. The shock waves were produced by impact of aluminum flyer plates accelerated explosively to velocities of 0.125 cm/μsec and 0.33 cm/μsec. Corresponding peak pressures in aluminum were 110 and 345 kbar, respectively. Free-surface velocities were measured for varying target thickness by observing with a streak camera the time of flight of a thin shim across a known gap. This technique gave higher precision than techniques employed previously.[5,6,7]

Reasonably accurate measurements of the elastic sound speeds of the shocked states were obtained for 2024-T351 aluminum; these permit values of the elastic shear modulus to be obtained.

Attempts to measure a complete particle-velocity profile by means of a fluid gage were not successful. Serious complications in the analysis of the experiments were introduced by changes of the refractive index with pressure and by possible spallation near the specimen surface. However, an independent measurement of the elastic sound speed was obtained at a pressure of 110 kbar in 2024-T351 aluminum that agrees very well with that deduced from free-surface measurements.

The data generated on 2024-T351 aluminum during the report period do not show a stepwise decrease in the free-surface velocity as predicted by the elastoplastic model with a von Mises (or Coulomb) yield criterion. Instead, the decay of peak velocity is continuous, implying that there is no distinct separation of elastic and plastic release waves. Earlier experiments with Manganin wire gages and optical

55

wedges showed similar behavior[5,6,7] but the evidence was not regarded as conclusive at that time.

The lack of separation of elastic and plastic relief waves is unfortunate since the stress relief due to the elastic wave is a measure of the yield strength under shock conditions, but it cannot be clearly identified in the data. The most probable explanation is that a Bauschinger effect tends to spread the elastic relief wave. This effect has been observed at lower pressures.[3]

The case for annealed 1060 aluminum is less clear. The data appear to show a step region, but more data, from thicker targets, are needed to establish its behavior.

An important result is that a significant difference is observed in the behavior of 2024-T351 and 1060 aluminum. The 1060 is clearly more fluid-like at high pressure. Thus a correlation is observed between the zero pressure and high pressure yield strengths.

The experimental results for Teflon agree reasonably well with predictions assuming fluid behavior; no pronounced elastoplastic effects are observed. The agreement shown is evidently partially fortuitous, however, since an assumption invoked in the data reduction is not completely accurate.* More information on the complete P-V-E equation of state for Teflon would permit a more definitive appraisal of the accuracy of the fluid model.

---

* The computed shock particle velocities are compared with one-half the measured free-surface velocities. This procedure is valid only where entropy can be neglected in the equation of state and material rigidity can be neglected. For Teflon the results indicate that this "doubling approximation" is not accurate.

DEFINITION OF SYMBOLS
IN APPENDIX I

n_1 Index of refraction of unshocked liquid

n_2 Index of refraction of shocked liquid

X Displacement of grid image in object space

β Angle through which the foil is turned by shock

α Angle between the shock front and the unturned foil

d Distance of the grid from the glass cover on the fluid cell

s Distance from the glass cover to the Mylar foil in the fluid cell

u_p Particle velocity in the shocked fluid

q_0 "Apparent velocity"--the velocity of the point of intersection of the shock and foil

U_s Shock velocity in the fluid

ρ_1 Initial density of the fluid

ρ_2 Shocked density of the fluid

J Displacement of grid line as measured on the film reader (jump in image space)

R_s Shot reduction factor = ratio of distance on the film reader to distance at the shot

D Effective standoff distance, $n_1 d + s$

APPENDIX I

IMMERSED FOIL ANALYSIS

The cell containing the inclined aluminized Mylar foil is mounted directly on the driving material in which a shock is induced. The fluid is added to immerse the foil completely. Small holes in the foil insure that the hydrostatic pressure is the same on both sides of the foil; this is necessary because any bowing of the foil changes the reflecting surface from plane to spherical, thus invalidating the following analysis. The light source and grid are arranged so that the streak camera views the images of the grid sources in the immersed foil (Fig. 22). The angle between the normal to the foil and the optic plane is assumed in all that follows to be so near zero that it can be neglected.
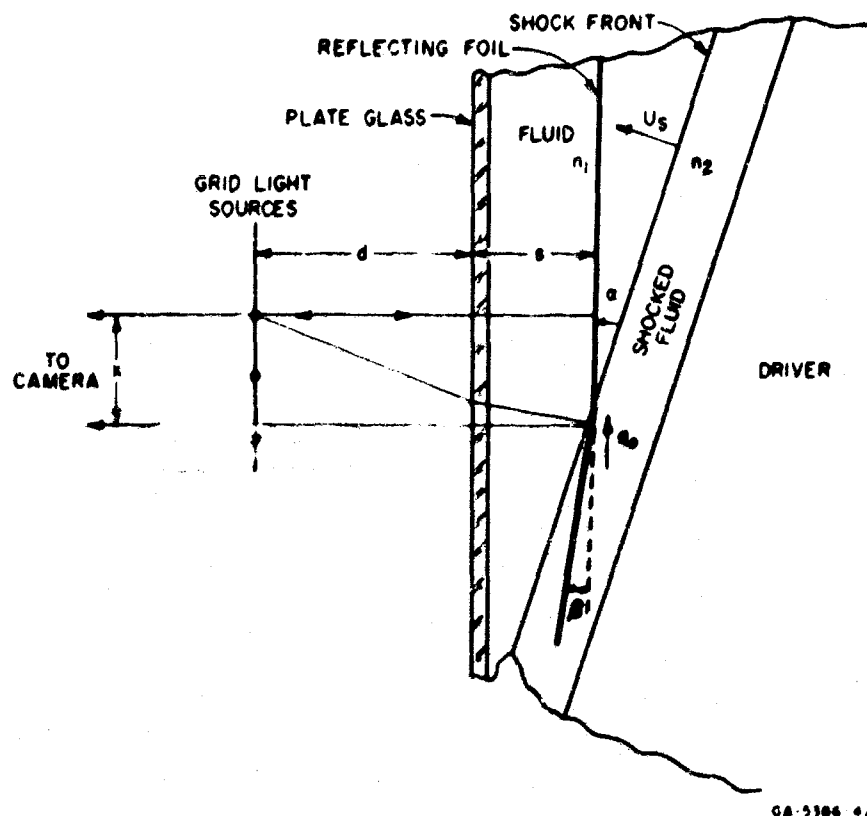
FIG. 22 SCHEMATIC VIEW OF IMMERSED FOIL GAGE (The angle between the shock front and the foil is α, and the foil is turned through an angle β. n_1 = the initial index of refraction and n_2 is the shocked refraction index.)

59

As the shock propagates into the liquid, it passes over the foil and imparts to it a velocity in the direction of the shock velocity. Because of the small thickness of the foil, the velocity of the foil soon becomes equal to the particle velocity of the shocked liquid. The effect of the moving, bent foil is to displace the images of the grid sources. As shown in Fig. 22, the new images are displaced toward the portion of the foil previously shocked. The displacement of the grid image along the direction parallel to the slit is called the jump, and is denoted as X .

Figure 11 is a streak camera record obtained with the use of an immersed foil cell. The shock entered the gage and was first detected at A . As the shock moved through the liquid, its intersection with the foil was indicated by the successive terminations of the original grid traces and the appearance of the displaced traces. This locus of end points is along the line AB. The original and displaced positions of Line 11 are denoted in the figure. This line displacement as recorded by the camera is proportional to the jump, X. Also note that the displaced grid sources are nearer to the driver specimen than the originals. There is also an interval of time when both the original and displaced images are photographed by the camera. This occurs because the displaced image can be observed in the turned foil prior to the arrival of the shock at the original position.

Figure 23 is a schematic of the shock front, turned Mylar foil, and the fluid cell cover. The ray from the grid source is refracted at the top of the cell, again at the shock front, and is then reflected off the Mylar foil back through the shock to emerge parallel to the optic plane. The distance the emerging ray is displaced from the original grid position is the jump X (the camera is considered to be effectively at infinity). Referring to the figure, it is evident that the jump can be written as

$$X = d \tan f + s_1 \tan \delta + s_0 [\tan(\alpha - c) - \tan(\alpha - a)] \qquad (24)$$
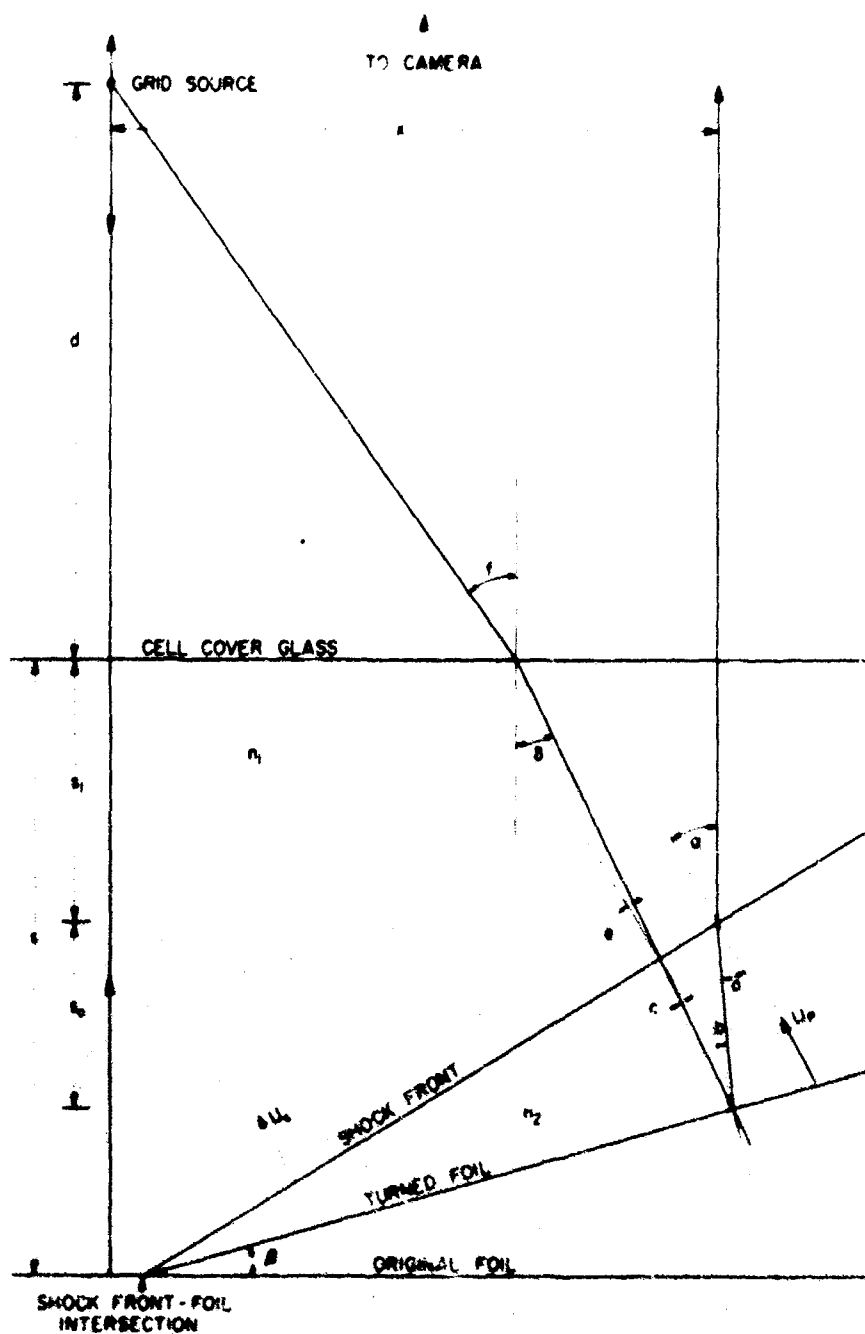
FIG. 23 SCHEMATIC OF RELATION BETWEEN SHOCK FRONT
AND FLUID CELL COMPONENTS

61

Write Snell's Law or each refraction

$$\sin f = n_1 \sin \delta \quad ,$$

$$n_1 \sin e = n_2 \sin c \quad , \tag{25}$$

$$n_1 \sin \alpha = n_2 \sin a$$

and, by consideration of the geometry, we can write:

$$\delta = \alpha - e$$

$$b = \beta - \alpha + a \tag{26}$$

$$c = \alpha - \beta - b$$

We wish to obtain a relationship between the turning angle β, the shock angle α, and the jump X. Note that when a displaced grid image is first seen in the turned foil, the depth of the shocked fluid between the foil and the shock is much less than the depth of unshocked fluid between the shock and the cell cover glass, so that the error introduced by replacing s_1 by s is small. It is also assumed that the shocked index is a constant in the region between the shock front and the turned foil and that s_0 can be neglected. Then Eq. (24) becomes

$$X = d \tan f + s \tan \delta \tag{27}$$

Using Eqs. (25) and (26)

$$X = n_1 d \sin \delta \left(1 - n_1^2 \sin^2 \delta \right)^{-1/2} + s \tan \delta \tag{28}$$

$$\delta = \alpha - \arcsin\left\{ \frac{n_2}{n_1} \sin\left[2\alpha - 2\beta - \arcsin\left(\frac{n_1}{n_2} \sin \alpha \right) \right] \right\} \tag{29}$$

When δ is substituted in Eq. (28) there results the desired expression relating X, n_1, n_2, α, and β.

The shock moving through the fluid imparts a particle velocity, u_p, to the fluid which is parallel to the shock velocity, U_s. Since the foil moves with the fluid, Fig. 24 can be constructed where q_0 is the apparent velocity, α is the angle between the shock and original foil, and β is the angle through which the foil turns. From the geometry of the figure we write

$$\frac{\sin\beta}{u_p} = \frac{\cos(\alpha-\beta)}{q_0} \qquad (30)$$

and

$$\sin\alpha = \frac{U_s}{q_0} \qquad (31)$$
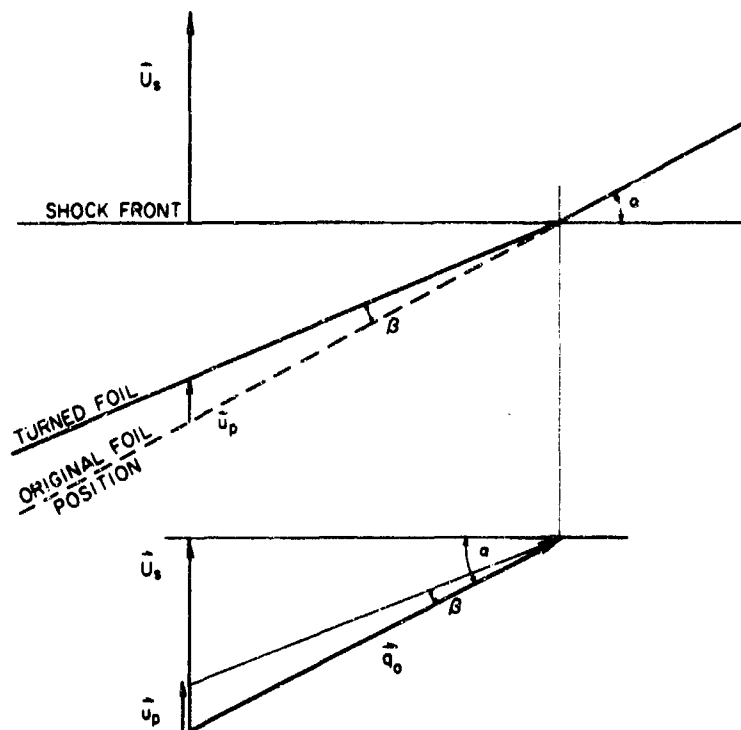
GA-5386-48

FIG. 24   RELATIONSHIP BETWEEN SHOCK VELOCITY $\vec{U}_s$, FLUID PARTICLE VELOCITY $\vec{u}_p$, APPARENT VELOCITY $\vec{q}_0$, SHOCK ANGLE α, AND TURNING ANGLE β

63

The set of equations(28-31) gives the relationships among the parameters that describe the interaction of the shock with the liquid and the foil. The apparent velocity q_0 and the jump X are both obtained from an analysis of the experimental film record, while the grid positions and cell dimensions are measured during assembly. It is then possible to determine either the particle velocity or the refractive index. If a knowledge of the refractive index is desired, then the fluid particle velocity must be inferred by an independent measurement; likewise, when using the technique to determine particle velocity, the refractive index must be known as a function of the shock state parameters.

1. Small Angle Approximation

When an experiment is performed in which the angles of interest in the foil analysis are small, i.e., $\sin \theta \doteq$ tangent $\theta \doteq \theta$, the following equations are applicable.

$$X = (n_1 d + s) \delta$$

$$\delta = 2\alpha \left[1 - \frac{n_2}{n_1}\right] + 2\beta \frac{n_2}{n_1} \tag{32}$$

and

$$\beta = \alpha \left[1 - \frac{n_1}{n_2}\right] + \frac{n_1}{n_2} \left(\frac{X}{2(s + n_1 d)}\right)$$

$$u_p = q_0 \beta \tag{33}$$

$$\alpha = \frac{U_s}{q_0} \tag{34}$$

Combining Eqs. (32), (33), and (34)

$$u_p = U_s \left(1 - \frac{n_1}{n_2}\right) + \frac{n_1}{n_2} \frac{q_0 X}{2(s + n_1 d)} \tag{35}$$

64

It has been found,[8,19] that the dependence of refractive index upon density is very nearly linear for some liquids.

$$n_2 = n_1 + k (\rho_2 - \rho_1) \tag{36}$$

From one-dimensional shock theory

$$\frac{u_p}{U_s} = 1 - \frac{\rho_1}{\rho_2} \tag{37}$$

Using Eqs. (36) and (37), Eq. (35) becomes

$$u_p = q_0 X / \left\{ 2(n_1 d + s) \left(1 - \frac{k\rho_1}{n_1} \right) \right\} \tag{38}$$

Therefore in an experiment either u_p or $k = dn/d\rho$ may be determined. When the dependence of n_2 on the shock parameters is not known, then the Hugoniot must be known to determine n_2. Along the Hugoniot, $u_p = u_p(U_s)$, and Eq. (35) may be solved for $n_2 = n_2 (u_p, q_0, X, \text{etc.})$. The particle velocity must then be determined by an independent means. In the shots where the flying plate velocity was measured, the particle velocity in the aluminum driver was known and the particle velocity in the fluid was found by impedance mismatching. The refractive index could then be calculated for the initial unattenuated shock. The dependence of the refractive index on density was assumed to be linear, so that the particle velocity could then be inferred after the shock had begun to attenuate. In experiments where the shocks were attenuating over the whole region of measurement, the previously determined refractive index function was employed.

2.   Large Angle Analysis

When the angles associated with the foil cell are large, so that the approximations of the previous section cannot be used, the working

65

equations are

$$X = n_1 d \sin \delta \left(1 - n_1^2 \sin^2 \delta\right)^{-1/2} + s \tan \delta \qquad (28)$$

$$\delta = \alpha - \arcsin\left\{\frac{n_2}{n_1} \sin\left[2\alpha - 2\beta - \arcsin\left(\frac{n_1}{n_2} \sin \alpha\right)\right]\right\} \qquad (29)$$

$$u_p = q_0 \sin \beta / \cos (\alpha - \beta) \qquad (30)$$

$$\alpha = \arcsin (U_s / q_0) \qquad (31)$$

Now define

$$z = \frac{1}{2} \left\{ \arcsin\left(\frac{n_1}{n_2} \sin \alpha\right) + \arcsin\left[\frac{n_1}{n_2} \sin (\alpha - \delta)\right] \right\} \qquad (39)$$

So Eq. (30) becomes

$$u_p = q_0 \frac{\sin (\alpha - z)}{\cos z} \qquad (40)$$

With a knowledge of refractive index and Hugoniot equation of state these equations can be solved to yield the particle velocity in terms of the apparent velocity and the grid line jump.

The experiments which employed large foil angles were designed so as to measure particle velocity over a substantial depth range in water. The calibration of refractive index was done with smaller angle foils and the results were applied to the large angle experiments. The relation

$$n_2 = n_1 + k (\rho_2 - \rho_1) \qquad (41)$$

was assumed to be sufficient. Using Eq. (37), Eq. (41) can be written

$$n_2 = n_1 + k \rho_1 (u_p / U_s - u_p) \qquad (42)$$

66

Water was the only fluid used and the equation of state was that of Rice and Walsh [20]

$$U_s = 1.483 + 25.306 \log \left[1 + u_p/5.190 \right] \tag{43}$$

where U_s and u_p have units of mm/μsec.

In order to obtain a solution to the set of equations above, a computer program was developed. The program solved Eq. (28) by an iterative process in order to find δ. Then by choosing a value for u_p it calculated in turn U_s, n_2, α, and z and compared the result of Eq. (40) with the initially chosen particle velocity. This process was repeated until the percent difference between the chosen and calculated particle velocity was less than 0.1 percent.

3. Film Record Reduction

Two quantities of interest are obtained from the photographic record: (1) the grid jump and (2) the velocity of the shock-foil intersection, i.e., the apparent velocity (see Fig. 11).

The jump is determined by measuring the distance on the film that the line is displaced and dividing by the appropriate reduction factor for the particular camera and film reading device used. The films on this project were read on a Telereadex instrument. The output of this machine is in counts proportional to distances on the film. It is then necessary to measure a known distance on the shot in order to determine the shot reduction factor R_s.

$$R_s = \frac{\text{Counts on the Telereadex}}{\text{Distance in mm on the shot}}$$

The distance to the camera objective is greater for the grid images than for the shot itself; consequently, the reduction factor for the grid images, R_g, is somewhat smaller than R_s. If L is the distance from

the shot to the objective lens, and D the effective standoff distance for the grid, then the ratio becomes

$$\frac{R_s}{R_g} = \frac{L + D}{L}$$

The magnitude of the jump as measured on the Telereadex is J. Therefore the actual jump magnitude is $X = J/R_g$.

The apparent velocity is inferred by a measurement of the slope of the line determined by the ends of the undisplaced traces (see Fig. 11). In general, it depends on the coordinate Z, or the distance from the apex. The angle between the vertical and the tangent to the cutoff curve is γ. Then the apparent velocity is

$$q_0 = \frac{W}{R_s} \cot \gamma$$

where W is the streak camera writing rate in counts/μsec as measured on the Telereadex.

When a film is analyzed, the positions of the undisplaced and displaced traces are recorded. These sets of data are then checked by first and second differences and smoothed by a computer program. The program also differentiates the data using three points and five points. It prints out the $\cot \gamma$ so that the apparent velocity can be calculated and the procedures for determining u_p as described above can be carried out.

Appendix II

INDEX OF REFRACTION MEASUREMENTS
AND DISCUSSION OF RELEVANT DIELECTRIC THEORY

The principal goal of a theory of dielectrics is to relate macroscopic quantities such as electric polarization, electric field, and electric susceptibility to microscopic concepts and quantities. These relations in general are functions of temperature, pressure, density, and the frequency of the applied electric field. Much work has been done developing both formal and physical theories for dielectric media. The purpose of this appendix is to review the basic ideas and problems involved in order to appreciate the significance of new data that have been obtained for the refractive index of a shocked dielectric.

1. General Concepts

A quantitative discussion involves the so-called electric polarization $\vec{P}$, which is equal to the electric dipole moment per unit volume, and its relation to the macroscopic electric field $\vec{E}$. Provided that the medium has no permanent polarization, that is that in the absence of an external electric field the average polarization is zero, then the polarization is a function of the applied field and can be expanded as a power series in the field. Experimentally it is found that the linear term in the expansion is adequate to describe physical systems wherein the electric field is not comparable to interatomic fields, which are on the order of 10^9 volts/cm. If the further simplification is made that the medium is isotropic so that the polarization is not dependent on the direction of the electric field with respect to the dielectric, we can write

$$\vec{P} = \chi_e \vec{E} \qquad (44)$$

where the proportionality constant χ_e is called the electric susceptibility. The first problem of the physical theory is to relate the

69

macroscopic quantity χ_e, or its equivalent the dielectric constant ϵ, to molecular quantities. Alternatively, since χ_e is defined by the above relation, the theory must relate $\vec{P}$ and $\vec{E}$ to molecular quantities.

The calculation of the local field is not simple; in fact, one of the central problems is to relate the local field $\vec{E}'$ to the macroscopic field $\vec{E}$. In only a few special cases can a simple relation between these two quantities be derived. Approximations to the local field will be discussed later.

In the case of $\vec{P}$, the problem is simple. Consider a molecule in a nonpolar dielectric, i.e., a dielectric in which the molecules do not have a permanent dipole moment. An electric field exists in the vicinity of the molecule due to an externally applied field. This local field is denoted as $\vec{E}'$ to keep it distinct from the external macroscopic field $\vec{E}$. The local field tends to polarize the molecule and the induced dipole moment is $\vec{p}$. Let $\langle \vec{p} \rangle$ be the mean value of the moment computed by the methods of statistical mechanics so that the desired polarization per unit volume is just

$$\vec{P} = N \langle \vec{p} \rangle \qquad (45)$$

where N is the number of molecules per unit volume.

When we relate microscopic quantities, we still cling to a linear relation between the local field and the extent to which the molecule is polarized. The proportionality constant, α, is called the polarizability and is a microscopic quantity. The molecules may have a permanent dipole moment due to the molecular charge distribution, so that the total moment is the sum of the permanent moment, $\vec{\mu}$, and the induced moment, $\alpha\vec{E}'$.

$$\vec{p} = \vec{\mu} + \alpha\vec{E}' \qquad (46)$$

It is convenient to consider α as the sum resulting from the contributions of several sources of polarization in the material. The main categories are labeled electronic polarization α_e, and atomic polarization α_a, so that $\alpha = \alpha_e + \alpha_a$. A concise outline of the several sources of polarization is given by Böttcher:[21]

70

"The average (dipole) moment, caused by the uniform external field, is the result of four different effects:

a. Rotation (orientation) effects.

   a1: The uniform (electric) field tends to direct the permanent dipoles (dipole orientation).

   a2: It also tends to direct an anisotropic particle into such a position that its axis of highest polarizability coincides with the direction of the external field. This effect may be neglected when the field is moderate.

b. Translation (deformation) effects.

   b1: The electrons are shifted relative to the positive charges (electronic polarization).

   b2: Atoms or atom groups are displaced relative to each other (atomic polarization).

The rotation effects are counteracted by the thermal movement of the molecules. Thus they are strongly dependent on the temperature, whereas the translation effects are only slightly dependent on the temperature, since they are intramolecular phenomena."

These classifications are convenient because the dielectric properties of a medium are dependent upon the frequency of the applied electric field. For static and low frequencies, all of these effects contribute to the polarization. As the frequency is increased to, say, the microwave region for water, the dipole orientation term becomes very important. At about 2×10^9 cycles/sec ($\lambda = 15$ cm) a resonance occurs which corresponds to the permanent dipoles of the water flipping back and forth in phase with the applied field. The dipole contribution becomes less important as the frequency is increased further. The molecules require a characteristic time to reorient themselves along the applied field, and when the frequency of the applied field becomes too large it changes considerably before the permanent dipoles are allowed to reach an equilibrium distribution. Hence, at optical frequencies the effect of the permanent dipole moment on the polarization is negligible.

Resonances also occur for the atomic effect. Depending on the material, resonant absorption due to atomic oscillations occurs at infrared or optical frequencies. Similarly, for the electronic component, resonances appear in the visible and ultraviolet. Therefore, the division of the polarizability, α, into its components is useful in understanding the basic physical phenomena that determine the dielectric properties within a particular frequency region.

2. Classical Microscopic Theory

A classical treatment of the problem can be given that exposes some of the essential features. Consider the displaceable electrical charges of the molecule (these charges may be the electrons or the atom groups) to be subject to a restoring force that is proportional to their displacement

$$\vec{F}_i = -k_i \vec{r}_i \qquad (47)$$

The electrostatic forces within the molecule provide the restoring forces. Let an electric field act on the charges. This field is external to the molecule but is identified with the local field in which the molecule finds itself, $\vec{E}'$. The equation of motion for the ith particle of charge e_i is

$$m_i \frac{d^2 \vec{r}_i}{dt^2} + k_i \vec{r}_i = e_i \vec{E}' \qquad (48)$$

where $e_i \vec{E}'$ is the external force on the ith particle. The natural frequency of the bound charge is $\omega_i = \sqrt{k_i/m_i}$ so that the equation of motion is rewritten

$$m_i \frac{d^2 \vec{r}_i}{dt^2} + m_i \omega_i^2 \vec{r}_i = e_i \vec{E}' \qquad (49)$$

For an impressed field of frequency $\omega/2\pi$ the solution is

$$\vec{r}_1 = \frac{e_1}{m_1(\nu_1^2 - \omega^2)} \vec{E}'$$

(50)

and the induced dipole moment is

$$\vec{p}_1 = e_1 \vec{r}_1$$

(51)

so the polarizability is

$$\alpha_1 = \frac{e_1^2}{m_1(\omega_1^2 - \omega^2)}$$

(52)

Since the polarizabilities are additive, the total molecular polarizability is

$$\alpha = \sum_i \frac{e_i^2}{m_i(\omega_i^2 - \omega^2)}$$

(53)

When the frequency of the external field approaches one of the natural frequencies of the system, $\omega = \omega_i$, a damping term must be included in the equation of motion. This treatment indicates the importance of the several α's in the vicinity of a resonance.

This classical result can also be obtained with the added condition of thermal agitation.[22] However, an exact treatment must consider other phenomena. The following discussion is by W. F. Brown, Jr.[23]

"The theory of dielectrics would be simple if the molecules...had no electrical effect on each other and if they were in static equilibrium. In fact, however, the molecules do not have any of these characteristics. There are three characteristics of actual molecular systems that complicate the problem: (1) they obey quantum laws; (2) they interact electrostatically; and (3) they are subject to thermal agitation.

If any single one of these factors is introduced, the theory becomes much more complicated. Introduction of quantum laws

73

(1) alone leads to the quantum-mechanical formula for polariz-
ability...; to evaluate the matrix elements...rigorously, it would
be necessary to solve the wave equation for each type of molecule
under consideration, and this is a formidable problem even for
only moderately complex molecules. Introduction of electrostatic
interactions (2) alone leads to the problem of evaluating the
local field intensity $\vec{E}'$ for a fixed configuration of molecules;
this problem has been solved rigorously only for crystal lattices
of certain types, and except in the simplest case (a cubic crystal)
the calculation requires rather elaborate mathematical techniques.
Introduction of thermal agitation (3) alone leads, however, to
a comparatively simple problem, one that can be solved by standard
techniques of statistical mechanics: for polar molecules, the
solution of this problem gives us Debye's theory.

If any two of the complication factors are introduced simultaneously,
the resulting problem could easily fill a book."[21],[24],[26]

Even though the situation may seem hopeless, we will show that with
some simplifying assumptions solutions can be obtained that predict
fairly well the observed phenomena.

3. The Local Field

We have shown that the macroscopic polarization $\vec{P}$ is simply related
to the microscopic dipole moment $\vec{p}$ [see Eq. (45)]. The local field, $\vec{E}'$,
is going to be the resultant of several fields. First, the externally
applied field, $\vec{E}$, contributes to the local field. It also polarizes
the medium so that there will be a contribution to the local field of
the reference molecule due to the polarization of its neighbors. If
the molecules have in addition a permanent dipole moment, the local
field is affected by dipole interactions with the applied field and
with the dipole field of the reference molecule. We therefore write
the local field as the sum of these various contributions.

$$\vec{E}' = \vec{E} + \sum_i \vec{E}_i$$

The problem is to evaluate the summation using some reasonable assump-
tions and models. The macroscopic relation between $\vec{P}$ and $\vec{E}$ [Eq. (44)]
is recast using the definition of the dielectric constant.

$$\vec{P} = \chi_e \vec{E} \qquad (44)$$

$$\epsilon = (1 + 4\pi\chi_e) \qquad (54)$$

Therefore

$$\vec{P} = \frac{\epsilon - 1}{4\pi} \vec{E} \qquad (55)$$

Equation (55) is valid for isotropic media with no permanent average polarization (units are cgs).

4. Low Density Model

The simplest model for calculating the local field is to consider it equal to the external field, i.e., the presence of the polarized neighbors has a negligible effect on the applied field. This situation may be realized in a low density gas. Consider the molecules to have no permanent dipole moment. The induced dipole moment is therefore

$$\langle \vec{p} \rangle = \alpha \vec{E}' = \alpha \vec{E} \qquad (56)$$

The polarization per unit volume is

$$\vec{P} = N \alpha \vec{E} \qquad (57)$$

Utilizing Eq. (55) the molecular polarizability is

$$\alpha = \frac{\epsilon - 1}{4\pi N} \qquad (58)$$

The use of the relation

$$N = \frac{N_o \rho}{M} \qquad (59)$$

where N_o is Avogadro's number, ρ is the mass density, and M is the molecular weight, results in the expression

$$(4\pi N_o) \alpha = \frac{M}{\rho} (\epsilon - 1) \qquad (60)$$

75

In order to give meaning to Eq. (60), the experimental values of $(\epsilon - 1)/\rho$ might be examined. If, for example, this quantity is constant, one may justly infer that α is also a constant provided the approximation $\vec{E}' = \vec{E}$ is valid for the densities involved.

This model can be extended to polar molecules with the use of statistical mechanics. We have for polar molecules

$$\vec{p} = \vec{\mu} + \alpha\vec{E}' \qquad (46)$$

The usual treatment is the following. First the contribution to the polarization is computed as if $\mu = 0$, which gives

$$\epsilon - 1 = (4\pi N)\alpha \qquad (58)$$

Second, the contribution due to the permanent dipole moment is calculated assuming no induced dipole moment and the result is

$$\epsilon - 1 = (4\pi N)\mu^2/3kT \qquad (61)$$

Third, these two contributions are added to give

$$\epsilon - 1 = 4\pi N\left(\alpha + \frac{\mu^2}{3kT}\right) \qquad (62)$$

This equation is called the Langevin-Debye equation. It predicts that for polar gases the quantity $(\epsilon - 1)/\rho$ should be linear in $1/T$. This is found to be a good approximation in many cases. Notable deviations are observed for carbon dioxide.[26]

5. High Density Model

A correction to the previous model is due to Lorentz.[27] In dense media, the local field is no longer equal to the applied field because the polarization of neighboring molecules contributes significantly to the local field. Consider a sphere of radius "a" about the molecule. The distance "a" is chosen to be small from a macroscopic point of view, but large microscopically. The contribution to the local field from

molecules external to the sphere, $\vec{E}_1$, can be calculated by using macroscopic methods. The contribution to $\vec{E}'$ from molecules within the sphere, $\vec{E}_2$, is difficult to calculate, for there we are forced to use microscopic methods.

The calculation of $\vec{E}_1$ is accomplished by considering the field at the center of a hollow sphere of radius "a" imbedded in a dielectric of uniform polarization $\vec{P}$. The resulting surface charge density on the sphere surface due to the polarization is $\sigma = -\vec{P} \cdot \vec{n}$ where $\vec{n}$ is a normal to the surface. The contribution to the local field at the sphere center from a small surface charge is

$$dE_1 = \frac{(P \cos \theta) \cos \theta}{a^2} dS \tag{63}$$

where the direction of dE_1 is parallel to $\vec{P}$. Upon integration we find that

$$\vec{E}_1 = \frac{4\pi}{3} \vec{P} \tag{64}$$

The total local field becomes

$$\vec{E}' = \vec{E} + \frac{4\pi}{3} \vec{P} + \vec{E}_2 \tag{65}$$

The evaluation of $\vec{E}_2$ has been done for very symmetric situations (Lorentz did it for cubic lattices) and found to be zero. When the molecules are not fixed in position, $\vec{E}_2$ is not generally zero; however, for this model, the approximation is that $\vec{E}_2 = 0$. Then for nonpolar dielectrics, the local field becomes

$$\vec{E}' = \vec{E} + \frac{4\pi}{3} \vec{P} \tag{66}$$

Using Eq. (55) we find that the internal field is related to the external field as

$$\vec{E}' = \left(\frac{\varepsilon + 2}{3}\right) \vec{E} \tag{67}$$

The average dipole moment is

$$\langle \vec{p} \rangle = \alpha \vec{E}' = \alpha \left(\frac{\epsilon + 2}{3} \right) \vec{E} \tag{68}$$

The polarization/unit volume becomes

$$\vec{P} = N \langle \vec{p} \rangle = \left(\frac{\epsilon - 1}{4\pi} \right) \vec{E} \tag{69}$$

The molecular polarizability is obtained by combining Eqs. (68) and (69). The result is

$$\alpha = \frac{M}{\rho} \left(\frac{3}{4\pi N_0} \right) \left[\frac{\epsilon - 1}{\epsilon + 2} \right] \tag{70}$$

where N is defined as in Eq. (59). This equation is known as the Clausius-Mosotti equation.

As described for the previous model, the contribution to α from the permanent dipole moment of the molecules can be included. The result is

$$\left(\frac{\epsilon - 1}{\epsilon + 2} \right) \frac{M}{\rho} = \frac{4\pi N_0}{3} \left(\alpha + \frac{\mu^2}{3kT} \right) \tag{71}$$

6. Optical Frequency Considerations

In order to relate these results to optical frequencies, the Maxwell relation $\epsilon = n^2$ is used. This equation is valid so long as the magnetic permeability of the dielectric is 1. This can be seen by considering the definition of refractive index

$$n = c/v \tag{72}$$

where v is the phase velocity of light waves with frequency f. The speed of light in a nonconducting medium is $c/\sqrt{\mu' \epsilon}$ where μ' is the magnetic permeability of the medium. Therefore

78

$$\epsilon = \frac{n^2}{\mu^2} \tag{73}$$

Upon substitution of $\epsilon = n^2$ in the Clausius-Mosotti equation we arrive at the Lorentz-Lorenz equation

$$\left(\frac{n^2 - 1}{n^2 + 2}\right)\frac{M}{\rho} = \frac{4\pi N_0}{3}\alpha \tag{74}$$

Since for most dielectrics the contribution to α from the alignment of permanent dipoles at optical frequencies is negligible, we are justified to drop the $\mu^2/3kT$ term in Eq. (71) and the Lorentz-Lorenz equation can be applied equally well to polar molecules.

A quick summary of the validity and limitations of Eq. (74) is given by W. F. Brown.[23]

"The Lorentz local-field formula...has been derived only for
a lattice of dipoles with cubic symmetry. The dipoles must
all have the same constant vector moment. Actual materials
deviate from this model in one or more of the following
respects: the molecules are not located at points of a
lattice; the fields of the molecules are not simple dipole
fields; the moments are not all the same; or the moments
vary (in magnitude or direction or both) with time. Con-
sequently, the Lorentz formula and the dielectric-constant
formula that follows from it...must be regarded only as
first approximations."

Böttcher[21] has made a correction to the Clausius-Mosotti equation that involves the "molecular radius" "a" for nonpolar molecules. His result is

$$\left(\frac{\epsilon - 1}{\epsilon + 2}\right)\frac{M}{\rho} = \frac{4\pi N_0}{3}\alpha\left[\frac{9\epsilon}{(\epsilon + 2)\left\{(2\epsilon + 1) - \frac{\alpha}{a^3}(2\epsilon - 2)\right\}}\right] \tag{75}$$

Although this equation predicts the behavior of some gases better than the Lorentz equation, some calculations by Orttung[28] using experimental data indicated that there was not a clear case for the corrected Böttcher result over the Lorentz formulation for liquid water.

79

The molecular refraction is defined as

$$R = \frac{M}{\rho}\left(\frac{n^2 - 1}{n^2 + 2}\right) \tag{76}$$

and is related to the molecular polarizability, α, through the Lorentz-Lorenz equation (subject of course to the limitations of the Lorentz equation). Since we are dealing with optical frequencies, the dominant component in the polarizability is the electronic component. Examination of R as a function of density for a particular dielectric may indicate the extent to which α is affected by changes in molecular spacing. To this end, Table V is reprinted from the Handbook of Physics.[29] A comparison of R is made for large changes in density for several materials. R_g and R_ℓ represent the molecular refraction for the gas and liquid phases, respectively. In the case of water vapor, R_g = 3.74 cc/mole and for water in the liquid phase, R_ℓ = 3.71 cc/mole. This corresponds to a change in density of almost 100,000. It may be expected that an additional increase in density by a factor of less than two in a shock compression will not affect greatly the constancy of the molecular refraction.

7. Present Experimental Results

Four experiments were performed (11,189; 11,190; 11,253; and 11,762) in which an aluminum flying plate impacted the aluminum cell bottoms of fluid gages. (See Section III for gage description.) The flying plate velocity was monitored with the use of "pin" switches. On Shot 11,762 the free surface velocity of the aluminum driver was also measured using the shim technique described in Section III. The peak shock-induced particle velocity in the water was determined graphically with the use of the Rice and Walsh[30] Hugoniot equation of state for the water.

Table VI lists the results of these experiments. The index of refraction listed and the shocked state densities were determined from the water gage records with the use of the computer program described in Appendix I. The dynamic gage measurements were all completed before any rarefaction waves had overtaken the shock front. The records themselves

Table V

MOLECULAR REFRACTIVITIES OF VARIOUS SUBSTANCES CALCULATED FROM GASEOUS- AND LIQUID-STATE DATA*

Substance	M	$(n_g - 1) \times 10^4$	n_l	ρ_l	R_g	R_l
Hydrogen, H_2	2	1.32	1.10	0.071	1.98	1.85
Water, H_2O	18	2.49	1.334	1.000	3.74	3.71
Ammonia, NH_2	17	3.73	1.325	0.616	5.60	5.54
Nitrogen, N_2	28	2.96	1.205	0.808	4.34	4.52
Oxygen, O_2	32	2.71	1.221	1.124	4.06	4.04
Nitric oxide, NO	30	2.97	1.330	1.269	4.45	4.83
Nitrous oxide, N_2O	44	5.16	1.193	0.870	7.74	6.24
Chlorine, Cl_2	71	7.73	1.367	1.33	11.58	11.92
Hydrochloric, HCl	36.5	4.47	1.245	0.95	6.71	5.95
Bromine, Br_2	160	11.32	1.659	3.12	17.00	15.30
Hydrobromic, HBr	81	5.73	1.352	1.630	8.57	10.72
Sulfur:						
S_2	64	11.11	1.929	2.04	16.6	14.9
H_2S	34	6.23	1.384	0.91	9.35	8.72
SO_2	64	6.90	1.410	1.359	10.32	11.61
CS_2	76	14.7	1.628	1.264	22.0	21.4
CO_2	44	4.49	1.192	0.796	6.74	6.78
Methanol, CH_2OH	32	5.49	1.331	0.794	8.24	8.23
Ethanol, C_2H_5OH	46	8.71	1.3623	0.800	13.05	12.72
Acetaldehyde, CH_3CHO	44	8.11	1.3316	0.800	12.16	11.40
Acetone, CH_3COCH_3	58	10.8	1.3589	0.791	16.20	16.05
Phosphorus, P_2	62	12.12	2.144	1.83	18.20	18.15

* The data refer to the Na D lines.

Source: Condon, E.H., and H. Odishaw, <u>Handbook of Physics</u>, McGraw-Hill, Inc., New York, 1958.

Table VI

RESULTS OF REFRACTIVE INDEX EXPERIMENTS

Shot Number	Flying Plate Velocity (cm/μsec)	Driver Free Surface Velocity (cm/μsec)	Fluid Particle Velocity[*] (cm/μsec)	Fluid Shock Velocity[†] (cm/μsec)	Initial Density (g/cm³)	Shocked State Density (g/cm³)	Initial Index of Refraction	Shocked Index of Refraction	$\frac{n - n_0}{\rho - \rho_0}$ (cm³/g)	Fluid Pressure (kbars)
11,159	0.132 ± .001	--	0.108 ± .001	0.356	0.998	1.433	1.333	1.507	0.40	38
11,160	0.135 ± .001	--	0.110 ± .001	0.360	0.998	1.437	1.333	1.504	0.39	39
11,233	0.127 ± .001	--	0.104 ± .001	0.349	0.998	1.422	1.333	1.494	0.38	36
11,703	0.130 ± .002	0.135 ± .001	0.103 ± .002	0.347	0.994	1.414	1.331	1.493	0.38	36

* Peak particle velocity in the fluid is determined by impedance matching methods.
† Reference 20: $U_s = 1.483 + 25.306 \log_{10} [1 + u_p/5.190]$. u_p and U_s in km/sec.

82

Table VII

MOLECULAR REFRACTION OF WATER:

$$R = \frac{M}{\rho}\left[\frac{n^2 - 1}{n^2 + 2}\right]$$

	State				Molecular
	Pressure (kbars)	Temperature[†] (°C)	Density (g/cc)	Refractive Index	Refraction (cc/mole)
Data from Present Study					
Shot number					
11,762	36	175	1.414	1.493	3.70
11,253	36	175	1.422	1.494	3.68
11,190	39	190	1.437	1.504	3.71
11,189	38	185	1.433	1.507	3.76
Atmospheric Pressure Data[30]					
Water					
Liquid	1×10^{-3}	20	0.9982	1.333	3.712
Ice	1×10^{-3}	-3	0.9164	1.3090[‡]	3.777
Vapor	1×10^{-3}	0	8×10^{-4}	1.000249	3.738
Data of Ahrens and Ruderman[9]					
Shot number					
10,640	48	240	1.468	1.474	3.45
10,383	58	295	1.515	1.482	3.39
10,640[§]	49	245	1.4907	1.5014	3.50
Data of Zel'dovich, et al.[19]					
--	39	190	1.43	1.47	3.51
--	110	635	1.67	1.53	3.33
--	144	890	1.75	1.56	3.33

* $M = 18.015$ g/mole

† Temperature from calculation of Rice and Walsh, Ref. 20.

‡ Ordinary ray.

§ Data reduction by present authors.

show that the initial relief waves do not pass over the immersed foil until after the jumps of the grid traces have been recorded.

Table VII lists the molecular refraction of water as calculated from the data obtained from the experiments mentioned and also data obtained from two other sources.[9,19] The average value of R for our four experiments is

$$R_{ave} = 3.71 \pm 0.03 \text{ cc/mole}$$

at a density of 1.43 ± 0.02 g/cc, which agrees very well with the value of R computed for water at 20°C and one atmosphere.

It appears that the electronic component of the molecular polarizability for water is little affected by the compacting of the molecules from a gaseous state to the densities realized at 38 kbars in the shocked liquid.

It is seen that there is some disagreement between our data and that of Ahrens and Ruderman[9] and Zel'dovich et al.[19] The disagreement between our data and that of Ahrens may be due to several possible sources: different techniques were used to determine the shock-induced particle velocity in the water; the present data were analyzed using the Rice and Walsh equation for water while the earlier data were reduced using a Hugoniot equation derived from the same experiment; random error.

Zel'dovich et al. quote a mean quadratic error in "n" of ± 0.01. However, the state in the shocked water was inferred by a measurement of shock velocity. Small errors in this measurement might account for the differences between their data and ours.

REFERENCES

1. Fowles, G. R., J. Appl. Phys. 32, 1475 (1961).

2. Lundergan, C. D. and W. Herrmann, J. Appl. Phys. 34, 2046-2053 (1963).

3. Barker, L. M., C. D. Lundergan, Walter Herrmann, J. Appl. Phys. 35, 1203-1212 (April 1964).

4. Jones, O. E. and J. R. Holland, J. Appl. Phys. 35, 1771-1773 (June 1964).

5. Curran, Donald R., J. Appl. Phys. 34, 2677-2685 (1963).

6. Erkman, J. O., Hydrodynamic Theory and High Pressure Flow in Solids, Stanford Research Institute, Project No. PGU-3712, Final Report, Contract No: DA-49-146-XZ-095, July 15, 1963.

7. Rempel, J. R. and J. O. Erkman, Shock Attenuation in Solid and Distended Materials, SRI Project GSU-4613, Final Report, WL-TR 64-119, August 31, 1965.

8. Allison, F. E., Mechanics of Hypervelocity Impact, Proceedings of 7th Hypervelocity Impact Symposium, Vol. 6 - Experiments, February 1965, p. 213.

9. Ahrens T. J. and M. H. Ruderman, Dynamic Properties of Rocks, Stanford Research Institute, Project GSU-4816, Interim Final Report, DASA-1694, April 30, 1965.

10. von Neumann, J. and R. D. Richtmyer, J. Appl. Phys. 21, 232 (1950).

11. Rice, M. H., R. G. McQueen, and M. Walsh, "Compression of Solids by Strong Shock Waves," Solid State Physics, Vol. 6, F. Seitz and D. Turnbull, eds., Academic Press, Inc., New York, 1958.

12. Fowles, G. R., J. Appl. Phys. 31, 655-661 (1960).

13. Wilkins, M. L., _Methods in Computational Physics_, Vol. 3, B. Alder, S. Feinbach, and M. Rotenberg, eds., Academic Press, New York and London, 1964.

14. Balchan, A. S. and G. R. Cowan, Rev. Sci. Instr. 35, 937-944 (1964).

15. Duvall, G. E. and G. R. Fowles, Chap. IX, Vol. II, _High Pressure Physics and Chemistry_, R. S. Bradley, ed., Academic Press, Inc., New York (1963).

16. Al'tshuler, L. V., S. B. Kormer, M. I. Brazhnik, L. A. Vladimirov, M. P. Speranskaya, A. I. Funtikov, Soviet Physics JETP 11, No. 4, (Oct. 1960).

17. Anderson, G. D., D. G. Doran, A. L. Fahrenbruch, "Equation of State of Solids: Aluminum and Teflon," Stanford Research Institute, Project GSU-5059, Final Report, Technical Report No. AFWL-TR-65-147, December 1965.

18. Netherwood, P. H., Ballistics Research Laboratory Memorandum Report No. 1626, December 1964.

19. Zel'dovich, Ya. B., S. B. Kormer, M. V. Sinitsyn, and K. B. Yushko, Soviet Physics Doklady 6, 494-496 (December 1961).

20. Rice, M. H. and J. M. Walsh, J. Chem. Phys. 26, 824-830 (1957).

21. Böttcher, C. J. F., _Theory of Electric Polarisation_, Elsevier Publishing Co., Amsterdam, The Netherlands, 1952.

22. Jackson, J. D., _Classical Electrodynamics_, John Wiley & Sons, Inc., New York, 1962.

23. Brown, W. F., Jr., _Handbuch der Physik_, Band XVII, pp. 1-154, Springer-Verlag, Berlin, 1956.

24. Van Vleck, J. H., _The Theory of Electric and Magnetic Susceptibilities_, Oxford University Press, 1932.

25. Frohlich, H., _Theory of Dielectrics - Dielectric Constant and Dielectric Loss_, Oxford University Press, 1949.

26. Michele, A. and L. Kleerekoper, Physica 6, 586 (1939); as quoted in Reference 21.

27. Lorentz, H. A., _The Theory of Electrons_, B. G. Teubner, Leipzig, 1909; Dover Publications, Inc., New York, 1952.

28. Orttung, W. J., J. Phys. Chem. 67, No. 2, 503-504 (1963).

29. Condon, E. U. and H. Odishaw, _Handbook of Physics_, McGraw-Hill, Inc., New York, 1958.

30. Dorsey, E. N., _Properties of Ordinary Water - Substance_, Reinhold Publishing Corp., New York, 1940.

DISTRIBUTION

DISTRIBUTION (cont'd)

No. cys

1	WLAS)
1	(WLAW)
1	(WLD)
1	(WLDC)
1	(WLDM)
1	(WLDN)
1	(WLR)
1	(WLRB)
1	(WLRE)
20	(WLRP)
2	(WLRT)
1	(WLX)
1	(WLS)
1	(WLF)

OTHER AIR FORCE AGENCIES

Director, USAF Project RAND, via: Air Force Liaison Office, The RAND Corporation, 1700 Main Street, Santa Monica, Calif 90406

1	(RAND Physics Div)
1	(RAND Library)
1	(ATTN: Dr. O. Nance)
1	(ATTN: D. McCloskey)
1	Hq OAR (RROS), Bldg T-D, Wash, DC 20333
1	AFOSR (SRGL), Bldg T-D, Wash, DC 20333
1	AFCRL, L.G. Hanscom Fld, Bedford, Mass 01731

ARMY ACTIVITIES

1	Chief of Research and Development, Department of the Army (Scientific and Technical Information Division, CRD/P), Wash, DC 20310
1	US Army Materiel Command, Harry Diamond Laboratories (ORDTL 06.33, Technical Library), Wash, DC 20438
1	ABGMA Liaison Office, Bell Telephone Laboratories, Whippany, NJ
1	Redstone Scientific Information Center, US Army Missile Command, (ATTN: Dr. J.P. Hallowes), Redstone Arsenal, Ala 35809
1	Director, Ballistic Research Laboratories (ATTN: Dr. R.J. Eichelberger), Aberdeen Proving Ground, Md 21005

DISTRIBUTION (cont'd)

Commanding Officer, Picatinny Arsenal, Dover, NJ 07801

1   (ATTN: Mr. Sam Stein)

1   (ATTN: Dr. Amina Nordio)

1   Commander, Army Munitions Command (AMSMV), Dover, NJ 07801

1   US Army Research Office, ATTN: Lt Gregory D. Atmore, Box CM, Duke
Station, Durham, NC

1   Director, Army Research Office, 3045 Columbia Pike, Arlington, Va 22204

1   Director, US Army Engineer Research and Development Laboratories,
ATTN: STINFO Branch, Ft Belvoir, Va 20260

1   Commander, NIKE-X Project Office, USAMC (ATTN: AMCPM-NXA, Capt Ogden),
Redstone Arsenal, Ala 35809

NAVY ACTIVITIES

1   Chief of Naval Research, Department of the Navy, Wash, DC 20390

1   Commanding Officer and Director, David Taylor Model Basin, Wash, DC

1   Commanding Officer and Director, Naval Applied Science Laboratory,
Brooklyn, NY

1   Commander, Naval Ordnance Laboratory, ATTN: Dr. Rudlin, White Oak,
Silver Spring, Md 20910

1   Director, Special Projects, Department of the Navy, Wash, DC 20360

1   Office of Naval Research, Wash, DC 20360

1   Director of Naval Warfare Analyses, Institute of Naval Studies,
Office of the Chief of Navy Ops, 545 Technology Square, Cambridge 39,
Mass

1   Commanding Officer, US Naval Weapons Evaluation Facility (NWEF,
Code 404), Kirtland AFB, NM 87117

OTHER DOD ACTIVITIES

2   Director, Defense Atomic Support Agency (Document Library Branch),
Wash, DC 20301

1   Director, Advanced Research Projects Agency, Department of Defense,
The Pentagon, Wash, DC 20301

1   Office of Director of Defense Research and Engineering, ATTN:
John E. Jackson, Office of Atomic Programs, Room 3E 1071, The Pentagon,
Wash, DC 20330

20   DDC (TIAAS), Cameron Station, Alexandria, Va 22314

AEC ACTIVITIES

1   US Atomic Energy Commission (Headquarters Library, Reports Section),
Mail Station G-017, Wash DC 20545

DISTRIBUTION (cont'd)

<u>No. cys</u>

Sandia Corporation, Box 5800, Sandia Base, NM 87115

1 (Information Distribution Division)

1 (L.M. Barker)

1 (C.D. Lundergan)

1 (R.A. Graham)

1 (W. Herrman)

1 (W.B. Benedick)

1 (G. Seay)

Sandia Corporation, Box 969, Livermore, Calif 94551

1 (Technical Library)

1 (T.B. Lane)

1 (Larry Bakken)

1 Chief, Division of Technical Information Extension, US Atomic Energy Commission, Box 62, Oak Ridge, Tenn 37831

1 University of California Lawrence Radiation Laboratory, ATTN: Director's Office (ATTN: R. Duff), P.O. Box 808, Livermore, Calif 94551

1 University of California Lawrence Radiation Laboratory (Technical Information Division, ATTN: Dr. R.K. Wakerling), Berkeley 4, Calif

Director, Los Alamos Scientific Laboratory, P.O. Box 1663, Los Alamos, NM 87554

1 (Helen Redman, Report Library)

1 (W. Deal/GMX-6)

1 (J. Taylor/GMX-6)

1 Brookhaven National Laboratory, Upton, Long Island, NY

1 Oak Ridge National Laboratory (Tech Library), Oak Ridge, Tenn 37831

1 Argonne National Laboratory, Library Services Dept, Report Section, Bldg 203, RM-CE-125, 9700 S. Cass Avenue, Argonne, Ill 60440

OTHER

1 Langley Research Center (NASA), ATTN: Associate Director, Langley Station, Hampton, Va

1 Manned Spacecraft Center (NASA), ATTN: Chief, Technical Information Division, Houston 1, Tex

1 Institute for Defense Analysis, Room 2B257, The Pentagon, Wash,DC 20330 THRU: ARPA

1 Research Analysis Corporation (Margaret L. Emerson, Librarian), McLean, Va 22101

1 Massachusetts Institute of Technology, Lincoln Laboratory (Document Library), P.O. Box 73, Lexington, Mass 02173

DISTRIBUTION (cont'd)

No. cys

1   Aerospace Corporation (ATTN: J. Lowry), P.O. Box 95085, Los Angeles 45, Calif

1   Aerospace Corporation, ATTN: Ali M. Naqvi, San Bernardino Operations, P.O. Box 1308, San Bernardino, Calif 92402

1   Applied Physics Laboratory, The Johns Hopkins University, 8621 Georgia Ave, Silver Spring, Md 20910

        AVCO Corporation, Research and Advanced Development Division, 201 Lowell Street, Wilmington, Mass

1   (ATTN: Chief Librarian)

1   (ATTN: M. Atkins)

1   (ATTN: J. Davis)

1   Forrestal Research Center Library, Aeronautical Sciences Bldg, Princeton University, Princeton, NJ

2   General Atomic Division, General Dynamics Corporation, 10955 John Jay Hopkins Drive, San Diego, Calif 92121

2   General Electric Co, MSD, ATTN: Dr. F.A. Lucy, Room M9505, P.O. Box 8555, Philadelphia 1, Pa

1   General Electric TEMPO, ATTN: DASA Data Center, 735 State Street, Santa Barbara, Calif

1   Massachusetts Institute of Technology, Division of Industrial Coopera- tion, 77 Massachusetts Ave, Cambridge, Mass

1   University of Illinois, Civil Engineering Dept, ATTN: Dr. N.M. Newmark, Talbot Laboratory, Urbana, Ill

1   University of Illinois, Eastern Experiment Station, US Bureau of Mines, College Park, Md

1   University of Michigan, University Research Security Office, Lobby 1, East Engineering Bldg, Ann Arbor, Mich

1   Space Technology Laboratories, Inc., AF Contr Mgt Office, c/o STLTD, Bldg S/1930, One Space Park, Redondo Beach, Calif 90278

1   University of Utah, Salt Lake City, Utah ATTN: Dr. S. Kistler

20   Stanford Research Institute, ATTN: Dr. Doran, Menlo Park, Calif 94025

        Boeing, Aero-Space Division, P.O. Box 3985, Seattle, Wash

1   (ATTN: D. Young)

1   (ATTN: G. Butler)

        Kaman Nuclear, Garden of the Gods Road, Colorado Springs, Colo

1   (ATTN: F. H. Shelton)

1   (ATTN: D. Williams)

1   Colorado School of Mines (ATTN: Prof J.D. Lubahn), Golden, Colo

DISTRIBUTION (cont'd)

No. cys

Washington State University, Pullman, Washington

1   (ATTN: Dr. G. Duvall)

1   (ATTN: Dr. G.W. Fowles)

Lockheed Missiles and Space Co., P.O. Box 504, Sunnyvale, Calif 94088

1   (ATTN: E.N. Perry, Dept 18-64, Bldg 153)

1   (ATTN: J.A. Whitman, Dept 8174, Bldg 153)

1   GCA, Inc, (ATTN: Dr. J. Ehrenfeld), Bedford, Mass

1   Physics International Corp, ATTN: Dr. W. Biernbaum, 2700 Merced St, San Leandro, Calif 94577

1   Shock Hydrodynamics, Inc (ATTN: R. Bjork), Sherman Oaks, Calif

1   Aerojet General Corp, ATTN: Dr. Fischer, 1171 Woodruff Ave, Downey, Calif

3   General Motors Defense Research Laboratories, ATTN: Dr. C. Maiden, Box T, Santa Barbara, Calif

1   Union Carbide Corp, ATTN: Dr. C. Zerby, P.O. Box 278, Tarrytown, N.Y. 10017

2   Nortronics, ATTN: Applied Research Dept, Mr. Bill Niles, 2323 Teller Road, Newbury Park, Calif

1   Manlabs, Inc, ATTN: Miss Roberta L. Barrar, Librarian, 21 Erie St, Cambridge 39, Mass

1   Emerson and Cuming, Inc, ATTN: Arthur J. Giguere, 604 182nd St, Gardenia, Calif 90247

1   Douglas Aircraft Corp, ATTN: S. Martinez, 3000 Ocean Park Blvd, Santa Monica, Calif 90406

1   Official Record Copy (Capt Crotwell/WLRP)

DOCUMENT CONTROL DATA - R&D

(Security classification of title, body of abstract and indexing annotation must be entered when the overall report is classified)

1 ORIGINATING ACTIVITY (Corporate author)	2a REPORT SECURITY CLASSIFICATION
Stanford Research Institute Menlo Park, California	Unclassified
	2b GROUP

3 REPORT TITLE

ATTENUATION OF SHOCK WAVES IN SOLIDS

4 DESCRIPTIVE NOTES (Type of report and inclusive dates)

Final Report   18 January 1965 to 2 March 1966

5 AUTHOR(S) (Last name, first name, initial)

Erkman, John O.; Christensen, Andrew B.; Fowles, G.R.

6 REPORT DATE	7a TOTAL NO. OF PAGES	7b NO. OF REFS
May 1966	112	30

8a CONTRACT OR GRANT NO.	9a ORIGINATOR'S REPORT NUMBER(S)
AF29(601)-6734	
b PROJECT NO. 5710	AFWL-TR-66-12
c Subtask No. 15.018	9b OTHER REPORT NO(S) (Any other numbers that may be assigned this report)
d.	SRI Project GSU-5386

10 AVAILABILITY/LIMITATION NOTICES This document is subject to special export controls and each transmittal to foreign governments or foreign nationals may be made only with prior approval of AFWL (WLRP), Kirtland AFB, N.M. 87117. Distribution is limited because of the technology discussed in this report.

11 SUPPLEMENTARY NOTES	12 SPONSORING MILITARY ACTIVITY
	Air Force Weapons Laboratory (WLRP) Kirtland AFB, New Mexico 87117

13 ABSTRACT

Attenuation of shock waves was studied in annealed 1060 aluminum, 2024-T351 aluminum, and Teflon by impacting samples with explosively driven aluminum plates. Free-surface velocities were measured as a function of target thickness by recording the time of flight across a known distance of a thin shim which was originally in intimate contact with the surface of the sample. A streak camera was used as the recording instrument. Experimental results are believed to be more accurate than any obtained previously. Samples of 2024-T351 aluminum were shocked to approximately 110 kbars and 340 kbars by flyer plates having velocities of about 0.125 cm/µsec and 0.33 cm/µsec, respectively. 1060 aluminum was shocked to 110 kbars and significant differences in its behavior were observed in comparison to the 2024-T351 aluminum. Two models are discussed for representing elastoplastic stress-strain relations. One of these models permits the yield stress to be an arbitrary function of the hydrostatic pressure. The other permits both the shear modulus and the yield stress to vary arbitrarily with the strain. Results of calculations using an artificial viscosity code are given for the two models. The experimental data do not show a stepwise decrease of the free-surface velocity as predicted by the simple elastic-plastic models with a von Mises or Coulomb yield criterion. This qualitative difference is attributed to Bauschinger effect. Results for Teflon indicate that the fluid model may be satisfactory although the data are meager and contain some inconsistencies.

DD FORM JAN 64 **1473**

14. KEY WORDS	LINK A		LINK B		LINK C	
	ROLE	WT	ROLE	WT	ROLE	WT
Shock propagation						
Shock attenuation						
Hugoniot						
Equation of state						
Dynamic response						
Solid materials						
Elastic plastic						

INSTRUCTIONS

1. ORIGINATING ACTIVITY: Enter the name and address of the contractor, subcontractor, grantee, Department of Defense activity or other organization (corporate author) issuing the report.

2a. REPORT SECURITY CLASSIFICATION: Enter the overall security classification of the report. Indicate whether "Restricted Data" is included. Marking is to be in accordance with appropriate security regulations.

2b. GROUP: Automatic downgrading is specified in DoD Directive 5200.10 and Armed Forces Industrial Manual. Enter the group number. Also, when applicable, show that optional markings have been used for Group 3 and Group 4 as authorized.

3. REPORT TITLE: Enter the complete report title in all capital letters. Titles in all cases should be unclassified. If a meaningful title cannot be selected without classification, show title classification in all capitals in parenthesis immediately following the title.

4. DESCRIPTIVE NOTES: If appropriate, enter the type of report, e.g., interim, progress, summary, annual, or final. Give the inclusive dates when a specific reporting period is covered.

5. AUTHOR(S): Enter the name(s) of author(s) as shown on or in the report. Enter last name, first name, middle initial. If military, show rank and branch of service. The name of the principal author is an absolute minimum requirement.

6. REPORT DATE: Enter the date of the report as day, month, year; or month, year. If more than one date appears on the report, use date of publication.

7a. TOTAL NUMBER OF PAGES: The total page count should follow normal pagination procedures, i.e., enter the number of pages containing information.

7b. NUMBER OF REFERENCES: Enter the total number of references cited in the report.

8a. CONTRACT OR GRANT NUMBER: If appropriate, enter the applicable number of the contract or grant under which the report was written.

8b, 8c, & 8d. PROJECT NUMBER: Enter the appropriate military department identification, such as project number, subproject number, system numbers, task number, etc.

9a. ORIGINATOR'S REPORT NUMBER(S): Enter the official report number by which the document will be identified and controlled by the originating activity. This number must be unique to this report.

9b. OTHER REPORT NUMBER(S): If the report has been assigned any other report numbers (either by the originator or by the sponsor), also enter this number(s).

10. AVAILABILITY/LIMITATION NOTICES: Enter any limitations on further dissemination of the report, other than those

imposed by security classification, using standard statements such as:

(1) "Qualified requesters may obtain copies of this report from DDC."

(2) "Foreign announcement and dissemination of this report by DDC is not authorized."

(3) "U. S. Government agencies may obtain copies of this report directly from DDC. Other qualified DDC users shall request through
_____."

(4) "U. S. military agencies may obtain copies of this report directly from DDC. Other qualified users shall request through
_____."

(5) "All distribution of this report is controlled. Qualified DDC users shall request through
_____."

If the report has been furnished to the Office of Technical Services, Department of Commerce, for sale to the public, indicate this fact and enter the price, if known.

11. SUPPLEMENTARY NOTES: Use for additional explanatory notes.

12. SPONSORING MILITARY ACTIVITY: Enter the name of the departmental project office or laboratory sponsoring (paying for) the research and development. Include address.

13. ABSTRACT: Enter an abstract giving a brief and factual summary of the document indicative of the report, even though it may also appear elsewhere in the body of the technical report. If additional space is required, a continuation sheet shall be attached.

It is highly desirable that the abstract of classified reports be unclassified. Each paragraph of the abstract shall end with an indication of the military security classification of the information in the paragraph, represented as (TS), (S), (C), or (U).

There is no limitation on the length of the abstract. However, the suggested length is from 150 to 225 words.

14. KEY WORDS: Key words are technically meaningful terms or short phrases that characterize a report and may be used as index entries for cataloging the report. Key words must be selected so that no security classification is required. Identifiers, such as equipment model designation, trade name, military project code name, geographic location, may be used as key words but will be followed by an indication of technical context. The assignment of links, rules, and weights is optional

AFSC (RAFB NM)